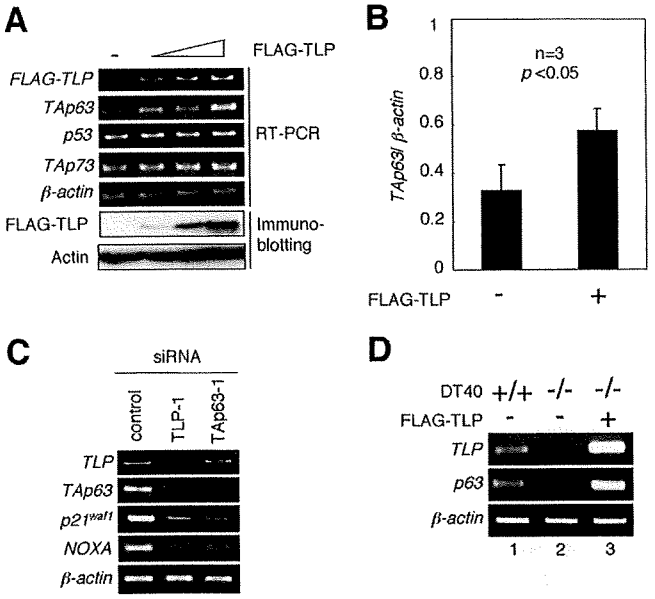

FIGURE 1. **Effects of ectopic expression of TLP on *p53* family members.** *A*, enforced expression of FLAG-TLP results in the up-regulation of *TAp63* but not of *p53* and *TAp73*. Human cervical carcinoma-derived HeLa cells were transiently transfected with or without the increasing amounts of FLAG-TLP expression plasmid (1.0, 1.5, or 2.0 μg). As a negative control, the empty plasmid (2.0 μg) was introduced into HeLa cells (−). Forty-eight hours after transfection, total RNA and whole cell lysates were prepared and analyzed by semi-quantitative RT-PCR using the indicated primers and immunoblotting with anti-FLAG antibody, respectively. For RT-PCR, *β-actin* was used as an internal control. For immunoblotting, actin was used as a loading control. *B*, quantitative real-time RT-PCR analysis. HeLa cells were transiently transfected with the constant amount of the empty plasmid or with the expression plasmid encoding FLAG-TLP (2.0 μg). Forty-eight hours after transfection, the expression levels of *TAp63* were examined by quantitative real-time RT-PCR using *β-actin* as an internal control. Data represent -fold induction of *TAp63* mRNA levels relative to those of *β-actin* mRNA. *C*, siRNA-mediated knockdown of the endogenous TLP. Human hepatocellular carcinoma-derived Hep3B cells were transiently transfected with 10 nM of control siRNA, siRNA against *TLP* (TLP-1) or with siRNA targeting *TAp63* (TAp63–1). Forty-eight hours after transfection, total RNA was prepared and subjected to semi-quantitative RT-PCR. *β-actin* was used as an internal control. *D*, a significant correlation between the expression levels of *TLP* and *TAp63*. Chicken wild-type DT40 cells and TLP-deficient DT40 cells were transiently transfected with the empty plasmid (−) or with the expression plasmid for FLAG-TLP (+). Forty-eight hours after transfection, total RNA was prepared and processed for semi-quantitative RT-PCR. *β-actin* was used as an internal control.

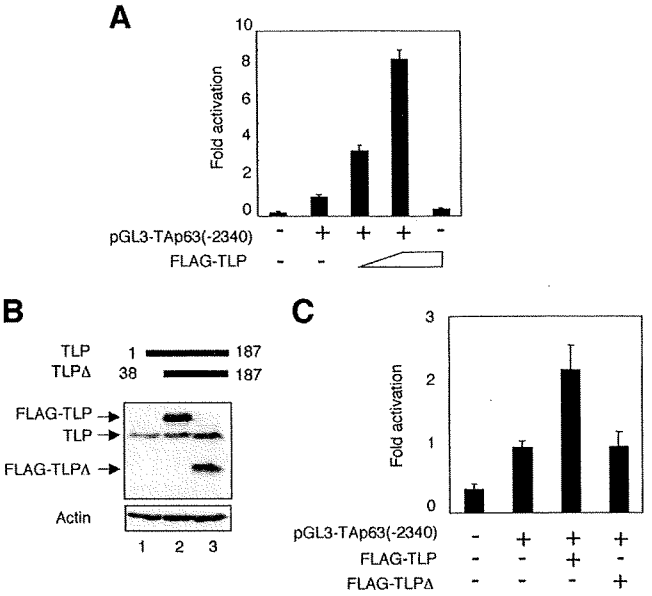

FIGURE 2. **NH_2-terminal deletion mutant of TLP fails to transactivate *TAp63* promoter.** *A*, pGL3-TAp63(−2340) responds to TLP. HeLa cells were transiently co-transfected with the constant amount of the luciferase reporter plasmid termed pGL3-TAp63(−2340) (100 ng) and *Renilla* luciferase reporter plasmid (pRL-TK, 10 ng) along with or without the increasing amounts of the expression plasmid encoding FLAG-TLP (100 or 200 ng). Forty-eight hours after transfection, cells were lysed and their luciferase activities were examined. Firefly luminescence signal was normalized based on the *Renilla* luminescence signal. Results are shown as -fold induction of the firefly luciferase activity compared with control cells transfected with the empty plasmid. *B*, immunoblotting. HeLa cells were transiently transfected with the constant amount of the empty plasmid (*lane 1*), the expression plasmid for FLAG-TLP (*lane 2*), or with the expression plasmid encoding FLAG-TLPΔ (*lane 3*). Forty-eight hours after transfection, whole cell lysates were analyzed by immunoblotting with the anti-TLP antibody. Actin was used as a loading control. *C*, luciferase reporter assay. HeLa cells were transiently co-transfected with the constant amount of pGL3-TAp63(−2340) and *Renilla* luciferase reporter plasmid along with or without the expression plasmid for FLAG-TLP or FLAG-TLPΔ. Forty-eight hours after transfection, cells were lysed and their luciferase activities were determined as in *A*.

expression of FLAG-TLP in *TLP*-deficient DT40 cells caused an increase in the expression level of *p63* (Fig. 1*D*). Thus, it is likely that *TAp63* is one of direct transcriptional target genes of TLP.

Identification of the Region within Human TAp63 Promoter Required for TLP-mediated Transactivation of TAp63—To identify the essential region within human *TAp63* promoter required for TLP-dependent transcriptional activation of *TAp63*, we have generated the luciferase reporter plasmid bearing *TAp63* genomic fragment spanning from positions −2340 to +26, where +1 represents the transcriptional initiation site, termed pGL3-TAp63(−2340). HeLa cells were transiently co-transfected with the constant amount of pGL3-TAp63(−2340), *Renilla* luciferase reporter plasmid together with or without the increasing amounts of the expression plasmid for FLAG-TLP. Forty-eight hours after transfection, cells were lysed, and their luciferase activities were measured. As shown in Fig. 2*A*, FLAG-TLP had an ability to enhance the luciferase activity driven by *TAp63* promoter in a dose-dependent manner. Similar results were also obtained in *p53*-deficient human lung carcinoma-derived H1299 cells (data not shown). In addition, NH_2-terminal deletion mutant of TLP (FLAG-TLPΔ) (Fig. 2*B*), which lacks a transcriptional activation function, failed to transactivate *TAp63* promoter as examined by luciferase reporter assay (Fig. 2*C*). These observations suggest that the genomic region of *TAp63* gene used in the luciferase reporter assay contains one or more TLP-responsive elements.

To further extend our study, a series of progressively 5′-truncated *TAp63* promoter reporter constructs were generated and subjected to luciferase reporter assay. As clearly shown in Fig. 3*A*, deletion up to −731 and −28 resulted in a significant decrease in the luciferase activity driven by *TAp63* promoter, indicating that there exist at least two independent genomic regions of *TAp63* gene (−1101 to −732 and −487 to −29) required for TLP-dependent transactivation of *TAp63*. To examine whether TLP could be recruited onto the essential genomic region of *TAp63* promoter, which we have identified, we performed a ChIP assay. For this purpose, we have designed four primer sets (#1, #2, #3, and #4) to amplify the indicated genomic regions of *TAp63* promoter (Fig. 3*B*). HeLa cells were

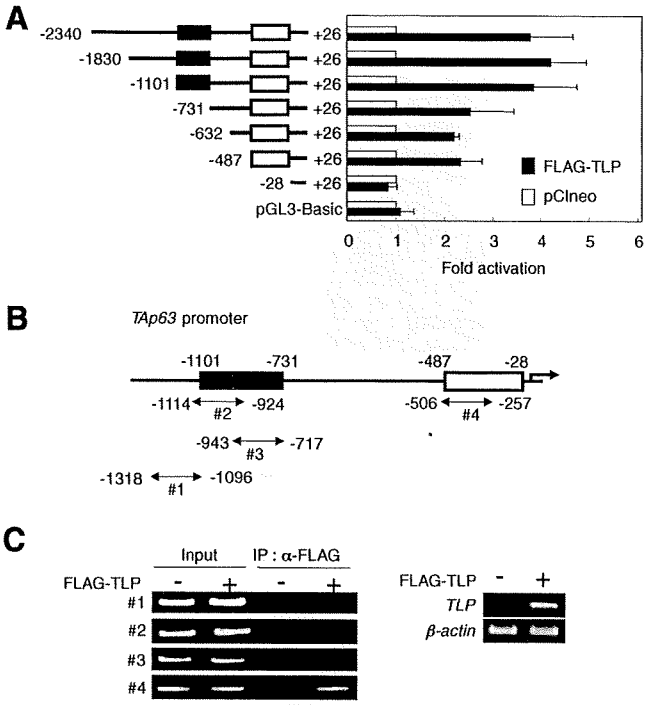

FIGURE 3. **Identification of region(s) within human *TAp63* promoter required for TLP-dependent transcriptional activation.** *A*, luciferase reporter assays. HeLa cells were transiently co-transfected with the constant amount of the indicated luciferase reporter constructs bearing various length of human *TAp63* promoter region (100 ng) and *Renilla* luciferase reporter plasmid (pRL-TK, 10 ng) together with the empty plasmid (pCIneo) or with the expression plasmid for FLAG-TLP. Forty-eight hours after transfection, cells were lysed and their luciferase activities were measured as described in the legend for Fig. 2. *Filled* and *open boxes* indicate the putative TLP-responsive regions within *TAp63* promoter. *B*, schematic drawing of *TAp63* promoter region. *Filled* and *open boxes* indicate the putative TLP-responsive regions within *TAp63* promoter. The positions of primer sets (*#1*, *#2*, *#3*, and *#4*) relative to the transcriptional initiation site (+1) used for ChIP assay are indicated. *C*, ChIP assay. HeLa cells were transiently transfected with the empty plasmid or with the expression plasmid for FLAG-TLP. Expression of *FLAG-TLP* was confirmed by semi-quantitative RT-PCR (*right panels*). Forty-eight hours after transfection, cells were cross-linked with formaldehyde and cross-linked chromatin was sonicated followed by immunoprecipitation with anti-FLAG antibody. Genomic DNA was purified from the immunoprecipitates and subjected to PCR using the indicated primer sets.

transiently transfected with the empty plasmid or with the expression plasmid for FLAG-TLP. Forty-eight hours after transfection, chromatin DNA was cross-linked and then processed for ChIP assay. The expression of the exogenous FLAG-TLP was examined by semi-quantitative RT-PCR (Fig. 3*C*, *right panel*). As clearly shown in Fig. 3*C*, genomic DNA extending from −506 to −257 was specifically amplified, suggesting that TLP is efficiently recruited onto the proximal promoter region of the human *TAp63* gene (−487 to −29) and that the upstream sequences (−1101 to −732) might act to enhance the function of the TLP-bound downstream sequences.

Identification of the Putative TLP-responsive Element within the Proximal Region of TAp63 Promoter—During the extensive search of the proximal region of human *TAp63* promoter, we have found out the sequence element (5′-AGCTGGAGCA-3′), which was also included within one of the TLP-binding sequences of *NF1* gene (5′-AGCTGAGAGCA-3′). Of note, this sequence element was well conserved among mouse, chicken, and dog *TAp63* promoter regions (over 80% sequence identity). To address the functional significance of this sequence element in the regulation of TLP-dependent transcriptional enhancement of *TAp63* gene, we have generated a luciferase reporter plasmid bearing mutant *TAp63* promoter in which the putative TLP-responsive element (5′-AGCTGGAGCA-3′) was substituted to the mutant sequence (5′-CTAGTGAGCA-3′) (pGL3-TAp63(−2340/M1)). HeLa cells were transiently transfected with the constant amount of pGL3-TAp63(−2340) or pGL3-TAp63(−2340/M1) along with the expression plasmid for FLAG-TLP or with the empty plasmid. As shown in Fig. 4*A*, introduction of mutations into the putative TLP-responsive element decreased the luciferase activity mediated by exogenously expressed FLAG-TLP, suggesting that this sequence element might act as a TLP-responsive element for the human *TAp63* gene.

To further confirm this issue, we have inserted four tandem repeats of the putative TLP-responsive element or mutant form of the putative TLP-responsive element into just upstream of *TAp63* core promoter region to give pGL3-TAp63-TLP-luc and pGL3-TAp63-M1-luc, respectively. As shown in Fig. 4*B*, luciferase reporter assays demonstrated that pGL3-TAp63-TLP-luc but not pGL3-TAp63-M1-luc responds to the exogenously expressed FLAG-TLP, suggesting that the putative TLP-responsive element found in the present study plays an essential role in the regulation of TLP-dependent transactivation of *TAp63*.

Etoposide-mediated Induction of TLP and TAp63 in p53-deficient Cells—It has been shown that TAp63 is induced in human hepatocellular carcinoma-derived *p53*-deficient Hep3B cells in response to etoposide and also involved in the promotion of apoptosis (25, 26). We therefore investigated the effects of etoposide on the expression level of TAp63 and TLP in Hep3B cells. To this end, Hep3B cells were exposed to etoposide at a final concentration of 50 μM. At the indicated time points after etoposide treatment, total RNA and whole cell lysates were prepared and subjected to semi-quantitative RT-PCR and immunoblotting, respectively. As shown in Fig. 5*A*, the expression level of the endogenous *TLP* was induced in response to etoposide in association with the up-regulation of *TAp63* as well as its transcriptional target genes such as $p21^{waf1}$, *14-3-3σ*, *NOXA*, *PUMA*, and *BAX*. Similarly, etoposide treatment led to a remarkable induction of the endogenous TLP protein as well as TAp63 protein and its target gene products, including $p21^{waf1}$ and NOXA (Fig. 5*B*). Similar results were also obtained in human hepatocellular carcinoma-derived HepG2 cells (supplemental Fig. S1).

Consistent with our previous observations (27), TLP accumulated in cell nucleus of Hep3B cells in response to etoposide as examined by immunoblotting (Fig. 5*C*). Similar results were also obtained in HepG2 cells (supplemental Fig. S1). Next, we sought to examine whether the endogenous TLP could be recruited onto *TAp63* promoter in response to etoposide. For this purpose, Hep3B cells were treated with or without 50 μM etoposide. Forty-eight hours after etoposide treatment, cells were cross-linked and the immunoprecipitated genomic DNA was subjected to ChIP assay. As shown in Fig. 5*D*, the endogenous TLP was induced to be recruited onto *TAp63* promoter region in response to etoposide. Because it has been shown that

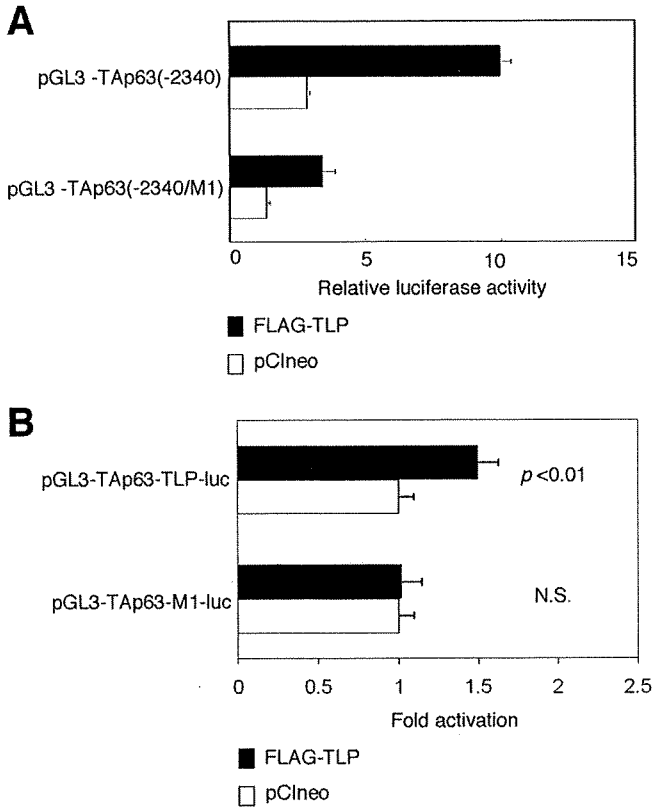

FIGURE 4. **TLP-responsive element within human *TAp63* promoter.** *A*, introduction of the mutations into the putative TLP-responsive element. We have introduced the mutations (5′-CTAGTGAGCA-3′) into the putative TLP-responsive element (5′-AGCTGGAGCA-3′) within pGL3-TAp63(−2340) to give pGL3-TAp63(−2340/M1). HeLa cells were transiently co-transfected with the constant amount of *Renilla* luciferase reporter plasmid together with pGL3-TAp63(−2340) or with pGL3-TAp63(−2340) in the presence of the expression plasmid for FLAG-TLP (*closed bars*) or empty plasmid (*open bars*). Forty-eight hours after transfection, cells were lysed and their luciferase activities were measured. *B*, functional significance of the putative TLP-responsive element. We have generated the luciferase reporter construct bearing four tandem repeats of the putative TLP-responsive element (5′-AGCTGGAGCA-3′) fused to just upstream of *TAp63* core promoter termed pGL3-TAp63-TLP-luc and its mutant carrying four tandem repeats of mutant form of the canonical TLP-responsive element (5′-CTAGTGAGCA-3′) fused to just upstream of *TAp63* core promoter termed pGL3-TAp63-M1-luc. HeLa cells were transiently co-transfected with the constant amount of *Renilla* luciferase reporter plasmid along with the constant amount of pGL3-TAp63-TLP-luc or with pGL3-TAp63-M1-luc in the presence of FLAG-TLP expression plasmid or the empty plasmid. Eighteen hours after transfection, cells were lysed, and their luciferase activities were determined. *Open* and *closed bars* indicate the relative luciferase activity in cells transfected with the empty plasmid and the expression plasmid for FLAG-TLP, respectively. *N.S.*, not significant.

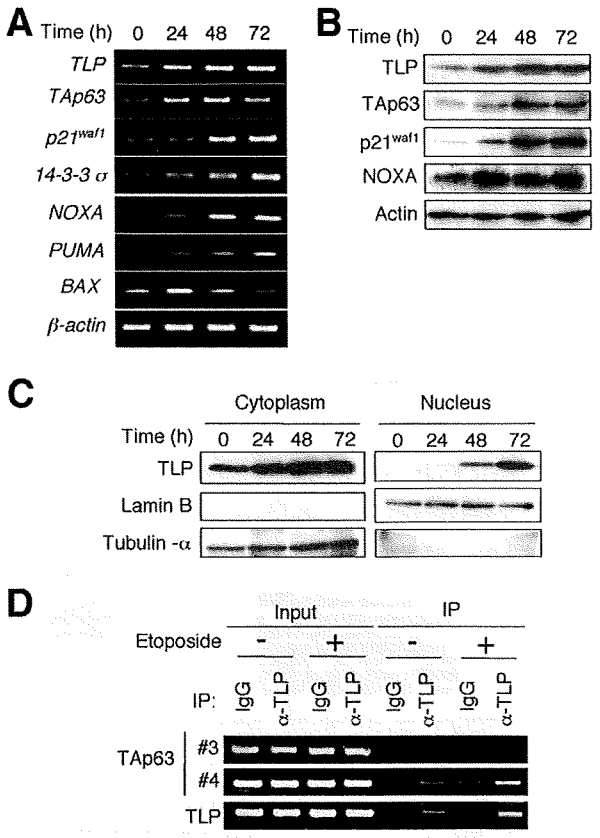

FIGURE 5. **TLP and TAp63 are induced in response to DNA damage.** *A*, etoposide treatment results in a significant induction of *TLP* and *TAp63*. Hep3B cells were treated with 50 μM of etoposide or left untreated. At the indicated time points after etoposide treatment, total RNA was prepared and subjected to semi-quantitative RT-PCR. *B*, immunoblotting. Hep3B cells were exposed to 50 μM of etoposide. At the indicated time points after exposure to etoposide, whole cell lysates were prepared and processed for immunoblotting with the indicated antibodies. *C*, etoposide-mediated nuclear accumulation of TLP. Hep3B cells were exposed to 50 μM etoposide. At the indicated time points after etoposide treatment, cells were biochemically fractionated into nuclear and cytoplasmic fractions followed by immunoblotting with anti-TLP antibody. Lamin B and tubulin-α were used as nuclear and cytoplasmic markers, respectively. *D*, ChIP assay. Hep3B cells were treated with 50 μM etoposide or left untreated. Forty-eight hours after etoposide treatment, cells were cross-linked with formaldehyde and cross-linked chromatin was sonicated followed by immunoprecipitation with normal goat IgG or with polyclonal anti-TLP antibody. Genomic DNA was purified from the immunoprecipitates and subjected to PCR using the indicated primer sets as described in the legend for Fig. 3.

TLP has an ability to transactivate its own promoter (28), we examined the recruitment of TLP onto its promoter region as a positive control (*bottom panel* of Fig. 5*D*).

The Effect of Knocking Down of the Endogenous TLP or TAp63 on Etoposide-mediated Apoptosis—To examine the functional significance of the endogenous TLP and TAp63 in the regulation of etoposide-mediated apoptosis, Hep3B cells were transiently transfected with control siRNA, siRNA against TLP (TLP-1), or with siRNA targeting TAp63 (TAp63–1). Forty-eight hours after transfection, cells were exposed to etoposide for 48 h. As seen in Fig. 6*A*, knocking down of the endogenous TLP resulted in a significant down-regulation of the endogenous TAp63 as well as its target gene products such as $p21^{waf1}$ and NOXA. Similarly, siRNA-mediated knockdown of the endogenous TAp63 caused a remarkable reduction in the expression level of $p21^{waf1}$ and NOXA, suggesting that the TLP/TAp63 pathway contributes to the promotion of apoptosis mediated by etoposide. Consistent with this notion, TUNEL staining experiments demonstrated that knocking down of the endogenous TLP or TAp63 results in a significant reduction of number of TUNEL-positive cells as compared with that of control cells (Fig. 5*B*). Similar results were obtained in Hep3B cells transfected with the different set of siRNA (supplemental Fig. S2) and also obtained in HepG2 cells (supplemental Fig. S3). Taken together, our present findings strongly suggest that TLP has an ability to induce etoposide-mediated apoptosis through up-regulation of TAp63 expression.

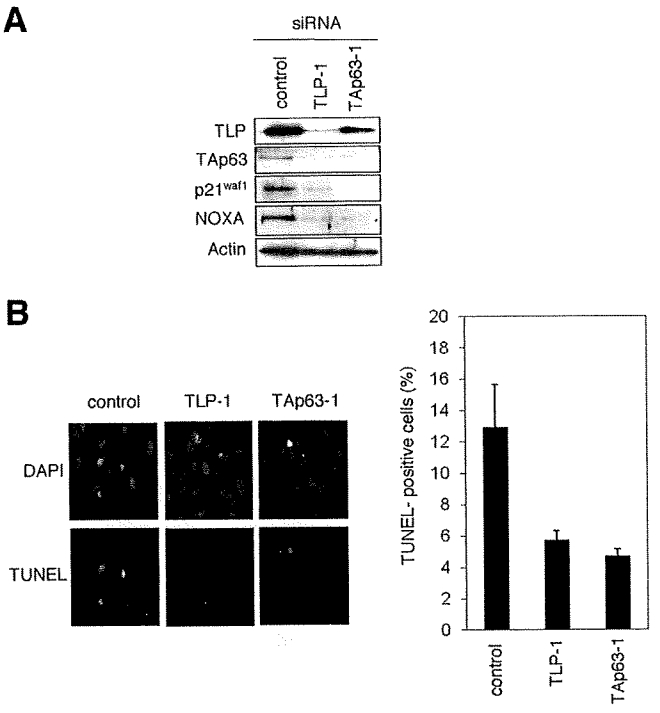

FIGURE 6. **Effects of the endogenous TLP and TAp63 in the regulation of DNA damage response.** *A*, siRNA-mediated knockdown of the endogenous TLP and TAp63. Hep3B cells were transiently transfected with 10 nM control siRNA, siRNA against *TLP* (TLP-1) or with siRNA targeting *TAp63* (TAp63-1). Forty-eight hours after transfection, cells were exposed to 50 μM etoposide. Forty-eight hours after etoposide treatment, whole cell lysates were prepared and processed for immunoblotting with indicated antibodies. *B*, TUNEL staining. Hep3B cells were transiently transfected as in *A*. Forty-eight hours after transfection, cells were exposed to 50 μM etoposide. Forty-eight hours after etoposide treatment, cells were fixed in 4% parafolmaldeyde and subjected to TUNEL staining. Cell nuclei were stained with 4′,6-diamidino-2-phenylindole (*DAPI*). The percentage of TUNEL-positive cells shown in each *column* represents the mean of three independent experiments (*right panels*).

DISCUSSION

Considering that TBP has an essential role in the regulation of basal transcription, TBP-related factors, including TLP might also participate in the transcriptional regulatory mechanisms. Previously, it has been shown that TBP is directly associated with tumor suppressor p53, and their complex formation contributes to the successful transcription (29). Although we have described that TLP has an intrinsic ability to prolong the G_2 phase and to induce apoptosis in a p53-independent manner (21), our earlier study did not rule out the possible involvement of the other p53 family members such as TAp73 and TAp63 in this process. In the present study, we have found for the first time that, upon DNA damage mediated by anti-cancer drug etoposide, TLP is induced to accumulate in cell nucleus in association with a significant up-regulation of *TAp63* as well as its direct target genes, suggesting that TLP acts as a transcriptional activator for pro-apoptotic TAp63.

According to our present results, ectopic expression of FLAG-TLP led to a significant induction of *TAp63* but not of the other *p53* family members such as *p53* and *TAp73*, indicating that TLP acts as a specific transcriptional activator for TAp63. Consistent with these observations, siRNA-mediated knockdown of the endogenous TLP resulted in a remarkable down-regulation of *TAp63*. In addition, TLP had an undetectable effect on SV40 promoter (data not shown). Intriguingly, TLP-dependent transcriptional up-regulation was also observed in chicken DT40 cells, suggesting that the molecular mechanisms behind TLP-dependent transcriptional up-regulation of *TAp63* are conserved among various species. By using luciferase reporter assays, we have identified the proximal and distal regions within human *TAp63* promoter required for TLP-dependent transcriptional activation of *TAp63*. Among them, TLP was efficiently recruited onto the proximal region but not onto the distal region as examined by ChIP assay. Thus, we have focused our attention on the proximal region for further analysis. Chong *et al.* described that TLP has an ability to transactivate *NF1* gene promoter, and they have identified the small independent two regions within *NF1* promoter required for TLP-dependent transcriptional activation of *NF1* gene (20). Based on their results, the above-mentioned two sequences directly bound to the purified TLP prepared from HeLa cells. During the extensive search of the proximal region of *TAp63* promoter, we have found out the sequence element (5′-AGCTGGAGCA-3′), which was also included within one of the TLP-binding sequences of *NF1* gene (5′-AGCTGAGAGCA-3′). Of note, this sequence element was well conserved among mouse, chicken, and dog *TAp63* promoter regions (over 80% sequence identity). Introduction of mutations into this sequence element decreased the luciferase activity mediated by exogenously expressed FLAG-TLP, suggesting that this sequence element might act as a TLP-responsive element for human *TAp63* gene.

As mentioned above, the distal region of *TAp63* promoter had an indirect effect on TLP-dependent transcriptional regulation of *TAp63*. Consistent with these results, pGL3-TAp63(−2340/M1) in which mutations were introduced into the proximal TLP-responsive element retained an ability to respond to the exogenously expressed FLAG-TLP but to the lesser degree. This might be due to the presence of the additional regulatory sequence(s) within *TAp63* promoter, including the distal region. When the four putative TLP-responsive elements were fused to core SV40 promoter, luciferase activity was undetectable in response to exogenously expressed FLAG-TLP (data not shown). In contrast, we have detected TLP-dependent luciferase activity driven by pGL3-TAp63-TLP-luc. Indeed, our luciferase reporter construct termed pGL3-TAp63(−487/+26) contained the proximal region and core *TAp63* promoter region, suggesting that there could exist a functional relationship between the proximal and core promoter regions with respect to TLP-dependent transcriptional regulation of *TAp63*. In support of this notion, both TLP and TBP have been shown to be recruited onto *NF1* genomic region containing TLP-responsive element and core promoter sequence (28). Further experiments should be required to adequately address this issue.

Another finding of our present study was that TLP is induced to accumulate in cell nucleus in response to etoposide, and contributes to etoposide-mediated apoptosis through the up-regulation of TAp63. Based on our present results, etoposide treatment promoted the efficient recruitment of the endogenous TLP onto *TAp63* proximal promoter region and resulted in a strong induction of *TAp63* as well as its direct target genes

implicated in apoptosis such as *PUMA*, *NOXA*, and *BAX*. siRNA-mediated knockdown of the endogenous TLP led to a significant down-regulation of TAp63 as well as pro-apoptotic NOXA. Additionally, knocking down of the endogenous TLP resulted in a remarkable inhibition of etoposide-mediated apoptosis as examined by TUNEL assay. Similar results were also obtained in *TAp63*-knocked down cells. In a sharp contrast, Lantner *et al.* found that CD74 stimulation leads to the activation of pro-survival NF-κB and then activated form of NF-κB transactivates TAp63 followed by TAp63-dependent up-regulation of anti-apoptotic Bcl-2 (30). Their observations indicated that NF-κB is one of transcriptional activators for TAp63; however, the up-regulation of TAp63 contributes to cell survival in mature B cells. The differential biological outcomes of the up-regulation of TAp63 might be due to the cellular contexts employed in the experiments. To our knowledge, our present result is a first finding showing that TLP acts as a transcriptional activator for pro-apoptotic TAp63 and participates in the regulation of DNA damage response. Thus, the TLP/TAp63 pro-apoptotic pathway is a novel one in response to DNA damage.

From the clinical point of view, several lines of evidence indicated that the altered expression of *p63* isoforms is observed in human tumor tissues (4), although loss of function mutations in *p63* are rarely detected in various human tumors (6, 7). For example, the dysregulation of the oncogenic *ΔNp63*, which is expressed from a different promoter than that used for expression of *TAp63*, was detectable, especially in squamous cell carcinomas (4, 31). In support with this notion, ΔNp63 contributes to cell survival through a dominant negative effect toward wild-type p53, TAp63, and TAp73 (4, 31). In contrast, the possible involvement of TAp63 in tumor generation might be attributed to its low expression levels in human primary tumors (32, 33). In this connection, higher expression levels of *TAp63* correlated with better prognoses of patients with bladder carcinoma (32). Thus, it is likely that TLP-TAp63 pathway might play an important role in certain tumor suppression. In accordance with this notion, it has been shown that TLP also induces the expression of *NF1*, a representative tumor suppressor gene (20). Given that etoposide stimulates nuclear accumulation of TLP and up-regulation of the *TAp63*, TLP-mediated *TAp63* expression followed by induction of apoptosis might help to suppress tumor generation.

Acknowledgments—We are grateful to Drs. Robert G. Roeder, Jeong H. Park, Tomoe Ichikawa, Miki Ohira, Yohko Nakamura, Hajime Kageyama, Cheng Hong, Kyoung-ae Park, and Tomoko Mabuchi for valuable discussion.

REFERENCES

1. Stiewe, T. (2007) *Nat. Rev. Cancer* **7,** 165–168
2. Yang, A., Kaghad, M., Wang, Y., Gillett, E., Fleming, M. D., Dötsch, V., Andrews, N. C., Caput, D., and McKeon, F. (1998) *Mol. Cell* **2,** 305–316
3. Osada, M., Ohba, M., Kawahara, C., Ishioka, C., Kanamaru, R., Katoh, I., Ikawa, Y., Nimura, Y., Nakagawara, A., Obinata, M., and Ikawa, S. (1998) *Nat. Med.* **4,** 839–843
4. Müller, M., Schleithoff, E. S., Stremmel, W., Melino, G., Krammer, P. H., and Schilling, T. (2006) *Drug Resist. Update* **9,** 288–306
5. Candi, E., Dinsdale, D., Rufini, A., Salomoni, P., Knight, R. A., Mueller, M., Krammer, P. H., and Melino, G. (2007) *Cell Cycle* **6,** 274–285
6. Hagiwara, K., McMenamin, M. G., Miura, K., and Harris, C. C. (1999) *Cancer Res.* **59,** 4165–4169
7. Sunahara, M., Shishikura, T., Takahashi, M., Todo, S., Yamamoto, N., Kimura, H., Kato, S., Ishioka, C., Ikawa, S., Ikawa, Y., and Nakagawara, A. (1999) *Oncogene* **18,** 3761–3765
8. Flores, E. R., Sengupta, S., Miller, J. B., Newman, J. J., Bronson, R., Crowley, D., Yang, A., McKeon, F., and Jacks, T. (2005) *Cancer Cell* **7,** 363–373
9. Flores, E. R., Tsai, K. Y., Crowley, D., Sengupta, S., Yang, A., McKeon, F., and Jacks, T. (2002) *Nature* **416,** 560–564
10. Levrero, M., De Laurenzi, V., Costanzo, A., Gong, J., Wang, J. Y., and Melino, G. (2000) *J. Cell Sci.* **113,** 1661–1670
11. Davidson, I. (2003) *Trends Biochem. Sci.* **28,** 391–398
12. Reina, J. H., and Hernandez, N. (2007) *Genes Dev.* **21,** 2855–2860
13. Ohbayashi, T., Kishimoto, T., Makino, Y., Shimada, M., Nakadai, N., Aoki, T., Kawata, T., Niwa, S., and Tamura, T. (1999) *Biochem. Biophys. Res. Commun.* **255,** 137–142
14. Teichmann, M., Wang, Z., Martinez, E., Tjernberg, A., Zhang, D., Vollmer, F., Chait, B. T., and Roeder, R. G. (1999) *Proc. Natl. Acad. Sci. U.S.A.* **96,** 13720–13725
15. Rabenstein, M. D., Zhou, S., Lis, J. T., and Tjian, R. (1999) *Proc. Natl. Acad. Sci. U.S.A.* **96,** 4791–4796
16. Perletti, L., Dantonel, J. C., and Davidson, I. (1999) *J. Biol. Chem.* **274,** 15301–15304
17. Moore, P. A., Ozer, J., Salunek, M., Jan, G., Zerby, D., Campbell, S., and Lieberman, P. M. (1999) *Mol. Cell. Biol.* **19,** 7610–7620
18. Ohbayashi, T., Shimada, M., Nakadai, T., Wada, T., Handa, H., and Tamura, T. A. (2003) *Nucleic Acids Res.* **31,** 2127–2133
19. Nakadai, T., Shimada, M., Shima, D., Handa, H., and Tamura, T. A. (2004) *J. Biol. Chem.* **279,** 7447–7455
20. Chong, J. A., Moran, M. M., Teichmann, M., Kaczmarek, J. S., Roeder, R., and Clapham, D. E. (2005) *Mol. Cell. Biol.* **25,** 2632–2643
21. Shimada, M., Nakadai, T., and Tamura, T. A. (2003) *Mol. Cell. Biol.* **23,** 4107–4120
22. Ichikawa, T., Suenaga, Y., Koda, T., Ozaki, T., and Nakagawara, A. (2008) *Oncogene* **27,** 409–420
23. Ohbayashi, T., Makino, Y., and Tamura, T. A. (1999) *Nucleic Acids Res.* **27,** 750–755
24. Ozaki, T., and Nakagawara, A. (2005) *Cancer Sci.* **96,** 729–737
25. Gressner, O., Schilling, T., Lorenz, K., Schulze Schleithoff, E., Koch, A., Schulze-Bergkamen, H., Lena, A. M., Candi, E., Terrinoni, A., Catani, M. V., Oren, M., Melino, G., Krammer, P. H., Stremmel, W., and Müller, M. (2005) *EMBO J.* **24,** 2458–2471
26. Petitjean, A., Cavard, C., Shi, H., Tribollet, V., Hainaut, P., and Caron de Fromentel, C. (2005) *Oncogene* **24,** 512–519
27. Park, K. A., Tanaka, Y., Suenaga, Y., and Tamura, T. A. (2006) *Mol. Cells* **22,** 203–209
28. Bush, S. D., Richard, P., and Manley, J. L. (2008) *Mol. Cell. Biol.* **28,** 83–92
29. Martin, D. W., Muñoz, R. M., Subler, M. A., and Deb, S. (1993) *J. Biol. Chem.* **268,** 13062–13067
30. Lantner, F., Starlets, D., Gore, Y., Flaishon, L., Yamit-Hezi, A., Dikstein, R., Leng, L., Bucala, R., Machluf, Y., Oren, M., and Shachar, I. (2007) *Blood* **110,** 4303–4311
31. Rocco, J. W., and Ellisen, L. W. (2006) *Cell Cycle* **5,** 936–940
32. Park, B. J., Lee, S. J., Kim, J. I., Lee, S. J., Lee, C. H., Chang, S. G., Park, J. H., and Chi, S. G. (2000) *Cancer Res.* **60,** 3370–3374
33. Koster, M. I., Lu, S. L., White, L. D., Wang, X. J., and Roop, D. R. (2006) *Cancer Res.* **66,** 3981–3986

nature genetics

FGF9 monomer–dimer equilibrium regulates extracellular matrix affinity and tissue diffusion

Masayo Harada[1,2], Hirotaka Murakami[3,11], Akihiko Okawa[3,11], Noriaki Okimoto[4,11], Shuichi Hiraoka[1,10,11], Taka Nakahara[5,10,11], Ryogo Akasaka[6,11], Yo-ichi Shiraishi[7,11], Noriyuki Futatsugi[4], Yoko Mizutani-Koseki[1], Atsushi Kuroiwa[7], Mikako Shirouzu[6], Shigeyuki Yokoyama[6,8], Makoto Taiji[4], Sachiko Iseki[5], David M Ornitz[9] & Haruhiko Koseki[1]

The spontaneous dominant mouse mutant, Elbow knee synostosis (*Eks*), shows elbow and knee joint synosotsis, and premature fusion of cranial sutures. Here we identify a missense mutation in the *Fgf9* gene that is responsible for the *Eks* mutation. Through investigation of the pathogenic mechanisms of joint and suture synostosis in *Eks* mice, we identify a key molecular mechanism that regulates FGF9 signaling in developing tissues. We show that the *Eks* mutation prevents homodimerization of the FGF9 protein and that monomeric FGF9 binds to heparin with a lower affinity than dimeric FGF9. These biochemical defects result in increased diffusion of the altered FGF9 protein ($FGF9^{Eks}$) through developing tissues, leading to ectopic FGF9 signaling and repression of joint and suture development. We propose a mechanism in which the range of FGF9 signaling in developing tissues is limited by its ability to homodimerize and its affinity for extracellular matrix heparan sulfate proteoglycans.

The fibroblast growth factors (FGFs) are widely expressed in developing and adult tissues and have diverse functions in organogenesis, tissue repair, nervous system control, metabolism and physiological homeostasis[1]. In humans and mice, the 22 FGF ligands are expressed in a spatiotemporally regulated manner and mediate signals through seven different isoforms of FGF receptors (FGFRs)[1]. The pharmacologic potential of FGF ligands has been highlighted by identification of gain-of-function mutations in genes encoding FGFRs 1–3 in individuals with chondrodysplasia and craniosynostosis syndromes[2,3]. These human diseases identify essential roles of FGF signaling not only in development but also in homeostasis of bones and joints.

Given these clinical, genetic and biochemical studies in humans and mice, the coordinated development of bones and joints seems to rely on precise FGFR signaling. This suggests that spatiotemporal constraints on FGF signaling are a prerequisite for appropriate functions *in vivo* and are indeed modulated at several distinct levels. First, the expression of FGF ligands is spatiotemporally restricted. Among the 22 FGF ligands, FGF2, FGF4, FGF7, FGF8, FGF9, FGF10, FGF17 and FGF18 are expressed in the limb bud and developing skeleton[4–6]. Of these, loss-of-function mutations have demonstrated that FGF2, FGF9 and FGF18 are involved in chondrogenesis and/or osteogenesis[7–10]. Induction of chondrodysplastic phenotypes by overexpression of FGF9 in mice also shows its ability to affect chondrogenesis[11]. Other elements implicated in FGF signaling are the heparan sulfate proteoglycans (HSPGs). Genetic studies in mice and *Drosophila melanogaster* suggest that HSPGs regulate the distribution and receptor binding of FGF ligands[12,13]. Finally, structural analyses of FGF9 suggest that it may form homodimers that could affect its ability to signal[14,15]. Because FGF9 homodimerization occludes several critical receptor binding sites, an autoinhibitory mechanism may function to modulate FGF9-dependent signal transduction. However, a functional demonstration of this proposed mechanism is lacking.

We have previously reported that a dominant mouse mutant, Elbow knee synostosis (*Eks*), shows radiohumeral and tibiofemoral synostosis, craniosynostosis (**Supplementary Fig. 1** online) and lung hypoplasia[16]. In this study, we identify a missense mutation that replaces Asn143 with threonine in the *Fgf9* gene in *Eks* mutant mice. We designate this mutant allele as $Fgf9^{Eks}$ and show that this mutation

[1]RIKEN Research Center for Allergy and Immunology, 1-7-22 Suehiro-cho, Tsurumi-ku, Yokohama, Kanagawa 230-0045, Japan. [2]Department of Immunology and [3]Department of Orthopaedic Surgery, Graduate School of Medicine, Chiba University, 1-8-1 Inohana, Chuo-ku, Chiba 260-8670, Japan. [4]RIKEN Advanced Science Institute, Computational Systems Biology Research Group, 61-1 Ono-cho, Tsurumi-ku, Yokohama, Kanagawa 230-0046, Japan. [5]Section of Molecular Craniofacial Embryology, Graduate School of Medical and Dental Sciences, Tokyo Medical and Dental University, 1-5-45 Yushima, Bunkyo-ku, Tokyo 113-8549, Japan. [6]RIKEN Systems and Structural Biology Center, 1-7-22 Suehiro-cho, Tsurumi-ku, Yokohama, Kanagawa 230-0045, Japan. [7]Division of Biological Science, Graduate School of Science, Nagoya University, Furo-cho, Chikusa-ku, Nagoya 464-8602, Japan. [8]Department of Biophysics and Biochemistry, Graduate School of Science, The University of Tokyo, 7-3-1 Hongo, Bunkyo-ku, Tokyo 113-0033, Japan. [9]Department of Developmental Biology, Washington University School of Medicine, 660 South Euclid Avenue, St. Louis, Missouri 63110, USA. [10]Present addresses: Department of Systems Biomedicine, National Research Institute for Child Health and Development, 2-10-1 Okura, Setagaya-ku, Tokyo 157-8535, Japan (S.H.) and Section of Developmental and Regenerative Dentistry, School of Life Dentistry at Tokyo, The Nippon Dental University, 1-9-20 Fujimi, Chiyoda-ku, Tokyo 102-8159, Japan (T.N.). [11]These authors contributed equally to this work. Correspondence should be addressed to H.K. (koseki@rcai.riken.jp).

Received 20 June 2008; accepted 22 December 2008; published online 15 February 2009; doi:10.1038/ng.316

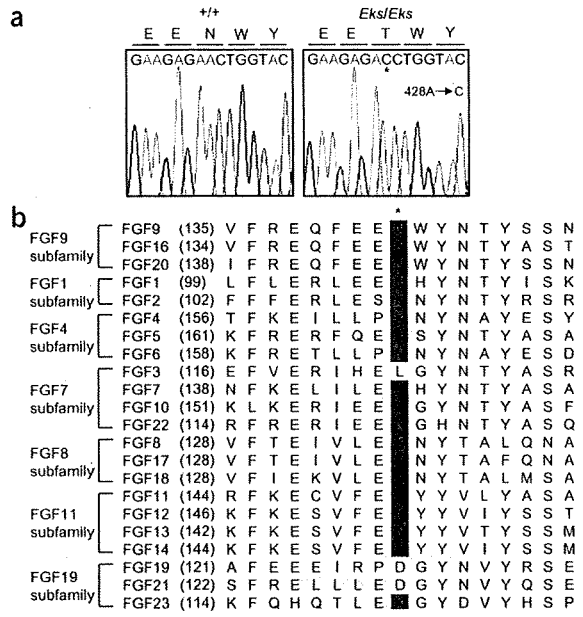

Figure 1 Missense mutation in the *Fgf9* gene of *Eks* mice. (**a**) Nucleotide sequence of the *Fgf9* cDNA derived from +/+ and *Eks/Eks* mice. *Eks* mutants have an A-to-C substitution at position 428, which results in the replacement of Asn143 with threonine. The *Eks* missense mutation is indicated by the asterisk, and the corresponding amino acid is shown in purple. (**b**) Structure-based sequence alignment of human FGFs. The amino acid sequence surrounding the N143T substitution in $FGF9^{Eks}$ and that of its corresponding domain in other human FGF family proteins are aligned on the basis of sequence identity. The Asn143 residue in FGF9 is highly conserved among most FGF proteins (purple box). The asterisk denotes the site of *Eks* mutation.

prevents homodimerization of FGF9, consequently decreasing the affinity of FGF9 for heparin. As a result, $FGF9^{Eks}$ is more diffusible in developing tissues, leading to ectopic FGF9 signaling in the prospective joints and sutures where it functions to repress development. Molecular-dynamics calculations suggest that the reduction in FGF9 affinity for heparin is due to the predominance of the monomeric form rather than to changes in its intrinsic affinity for heparin. We thus propose a mechanism in which the range of FGF9 signaling in developing tissues is limited through regulation of its affinity for HSPGs, which is at least in part controlled by the FGF9 monomer–dimer equilibrium. These observations could have far-reaching implications for the pharmacologic manipulation of FGF signaling under a variety of circumstances and in a wide range of tissues.

RESULTS

Eks is caused by a missense mutation in *Fgf9*

The *Eks* mutation was mapped between the polymorphic markers *D14Mit62* and *D14Mit5* on mouse chromosome 14 (ref. 16). Among 169 genes located in this interval, *Fgf9* seemed a likely candidate for the *Eks* mutation because FGF9 is a ligand for FGFR2c and FGFR3c[17] and is expressed in the developing limbs, cranial sutures and developing lung[8,18,19]. Sequence analysis of *Fgf9* cDNA from homozygous *Eks* mice revealed an A-to-C substitution at position 428, which resulted in the replacement of Asn143 with threonine (**Fig. 1a**). Notably, the Asn143 residue in FGF9 is highly conserved among most FGF proteins (**Fig. 1b**) and is predicted to be a critical amino acid residue for homodimerization and receptor binding[14,15].

We used a genetic approach to determine whether the N143T substitution in *Fgf9* was responsible for the *Eks* phenotype. We observed a mendelian pattern of inheritance of the mutation among 976 offspring of *Eks* heterozygous ($Fgf9^{Eks/+}$) matings, with heterozygous mice showing mild skeletal phenotypes and homozygous $Fgf9^{Eks/Eks}$ littermates showing severe skeletal phenotypes. The *Eks* phenotype and the mutation in *Fgf9* cosegregated in all cases. The absence of recombination between *Eks* and *Fgf9* among nearly 2,000 meiotic events provides strong evidence that the *Eks* mutation is allelic with *Fgf9*.

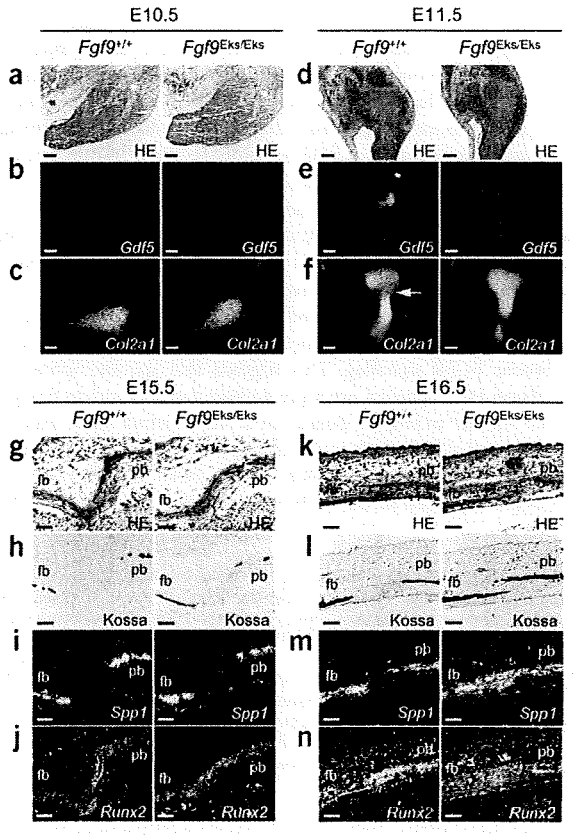

Figure 2 Synostotic phenotypes in $Fgf9^{Eks/Eks}$ mice. (**a–f**) Defects in early specification of prospective elbow joints in $Fgf9^{Eks/Eks}$ embryos. Hematoxylin and eosin staining (**a,d**) and *in situ* detection of *Gdf5* (**b,e**) and *Col2a1* (**c,f**) in the forelimb buds of $Fgf9^{+/+}$ and $Fgf9^{Eks/Eks}$ embryos at E10.5 and E11.5. In $Fgf9^{+/+}$ embryos, there was *Gdf5* expression at the prospective elbow joint (**e**, left), which was demarcated as the gap of *Col2a1* expression (**f**, arrow), at E11.5. In $Fgf9^{Eks/Eks}$ embryos, there was not *Gdf5* expression at the prospective elbow joint (**e**, right). Scale bars, 100 μm. (**g–n**) Ectopic osteogenesis at the coronal sutures in $Fgf9^{Eks/Eks}$ fetuses. Hematoxylin and eosin staining (**g,k**) and von Kossa staining (**h,l**) and *in situ* detection of *Spp1* (**i,m**) and *Runx2* (**j,n**) in the coronal suture of $Fgf9^{+/+}$ and $Fgf9^{Eks/Eks}$ fetuses at E15.5 and E16.5. Note the ectopic ossification in the suture of $Fgf9^{Eks/Eks}$ at E16.5. fb, frontal bone; pb, parietal bone. Scale bars, 100 μm.

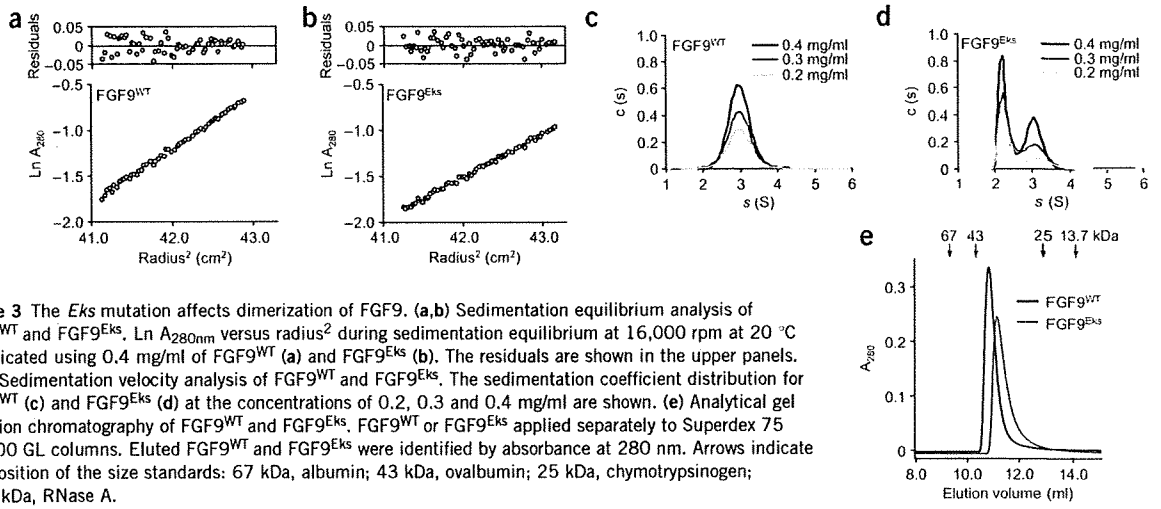

Figure 3 The *Eks* mutation affects dimerization of FGF9. (**a**,**b**) Sedimentation equilibrium analysis of $FGF9^{WT}$ and $FGF9^{Eks}$. Ln A_{280nm} versus radius^2 during sedimentation equilibrium at 16,000 rpm at 20 °C is indicated using 0.4 mg/ml of $FGF9^{WT}$ (**a**) and $FGF9^{Eks}$ (**b**). The residuals are shown in the upper panels. (**c**,**d**) Sedimentation velocity analysis of $FGF9^{WT}$ and $FGF9^{Eks}$. The sedimentation coefficient distribution for $FGF9^{WT}$ (**c**) and $FGF9^{Eks}$ (**d**) at the concentrations of 0.2, 0.3 and 0.4 mg/ml are shown. (**e**) Analytical gel filtration chromatography of $FGF9^{WT}$ and $FGF9^{Eks}$. $FGF9^{WT}$ or $FGF9^{Eks}$ applied separately to Superdex 75 10/300 GL columns. Eluted $FGF9^{WT}$ and $FGF9^{Eks}$ were identified by absorbance at 280 nm. Arrows indicate the position of the size standards: 67 kDa, albumin; 43 kDa, ovalbumin; 25 kDa, chymotrypsinogen; 13.7 kDa, RNase A.

Fgf9$^{Eks/Eks}$ mice phenocopy *Fgfr* gain-of-function mutants

Eks is a dominant mutation and joint synostosis and premature fusion of sutures have also been reported in mice expressing gain-of-function alleles of *Fgfr1* (ref. 20) and *Fgfr2c* (*Fgfr2*^{C342Y})[21]. Furthermore, homozygous *Fgf9* null mutants (*Fgf9*$^{-/-}$) show rhizomelia but not joint or suture synostosis[8]. Thus, we hypothesized that *Fgf9*^{Eks} encodes a gain-of-function mutation. To test this possibility, we first investigated whether there were phenotypic similarities between *Eks* mutants and gain-of-function mutants for *Fgfr1* and *Fgfr2*^{C342Y}. As initiation of elbow joint development was primarily impaired in *Fgfr1* gain-of-function transgenic mice[20], we examined radiohumeral joint development in *Fgf9*$^{Eks/Eks}$ mice (**Fig. 2a–f**). *Gdf5* (ref. 22) and *Col2a1* (ref. 23) demarcate the prospective elbow joint and cartilaginous condensation, respectively. *Gdf5* expression in the prospective joint space was observed as early as embryonic day E11.5 in *Fgf9*$^{+/+}$ control mice, but was completely absent in *Fgf9*$^{Eks/Eks}$ mice (**Fig. 2e**). Analysis of the prospective cartilage revealed a gap of *Col2a1* expression at the prospective elbow joint in E11.5 wild-type embryos (**Fig. 2f**, left). The gap of *Col2a1* expression was absent in *Fgf9*$^{Eks/Eks}$ mice (**Fig. 2f**, right). In summary, ectopic chondrocyte differentiation in the prospective elbow joint of *Fgf9*$^{Eks/Eks}$ mice seems very similar to that seen in transgenic mice that ectopically express an activated *Fgfr1* kinase domain in the presumptive joint field[20].

Premature fusion of coronal sutures in *Fgfr2*^{C342Y} mice results from excess osteogenic differentiation within the coronal suture mesenchyme[21]. To determine whether *Fgf9*$^{Eks/Eks}$ mice had similar histological features, we examined mineralization and the expression of the early osteoblast differentiation markers *Spp1* (ref. 24) and *Runx2* (ref. 25) in the coronal suture (**Fig. 2g–n**). At E15.5, both wild-type and *Fgf9*$^{Eks/Eks}$ mice showed similar coronal suture histology (**Fig. 2g–j**). However, at E16.5 von Kossa staining revealed considerably more overlap of the frontal and parietal bones in *Fgf9*$^{Eks/Eks}$ mice compared to *Fgf9*$^{+/+}$ mice (**Fig. 2l**). *Spp1* expression domains, which demarcate preosteoblasts and osteoblasts, showed wide separation of the frontal and parietal bones in *Fgf9*$^{+/+}$ mice; however, there was overlap in the *Fgf9*$^{Eks/Eks}$ mice (**Fig. 2m**). *Runx2* is highly expressed in immature osteoblasts at the leading edge of the frontal and parietal bones in *Fgf9*$^{+/+}$ mice (**Fig. 2n**, left). In E16.5 *Fgf9*$^{Eks/Eks}$ mice, the intensity of *Runx2* expression in the coronal suture was lower than in *Fgf9*$^{+/+}$ mice (**Fig. 2n**, right), suggesting premature differentiation of the osteoblasts at the presumptive suture. These phenotypes reflect abnormal osteogenic differentiation within the coronal suture mesenchyme and indicate that the defect in suture development occurs before E16.5. Taken together, these observations suggest that the $FGF9^{Eks}$ altered protein mediates excess FGFR signals within the prospective joints and sutures, preventing joint formation and promoting the fusion of cranial sutures.

The *Eks* mutation impairs homodimerization of FGF9

The predicted involvement of the Asn143 residue in homodimerization and receptor activation[14,15] suggests that changes in these processes may account for the apparent gain-of-function activity of the $FGF9^{Eks}$ altered protein. Homodimerization of FGF9 has been proposed to occlude receptor binding sites and consequently mediate an autoinhibitory mechanism for FGF9 signaling. We thus hypothesized that the *Eks* mutation might impair the autoinhibition. To test this possibility, we compared the degree of homodimerization of wild-type ($FGF9^{WT}$) and $FGF9^{Eks}$ proteins by analytical ultracentrifugation. $FGF9^{WT}$ and $FGF9^{Eks}$ were expressed in *Escherichia coli* and purified by column chromatography (**Supplementary Methods** and **Supplementary Fig. 2** online).

The molecular mass and association constant of $FGF9^{WT}$ and $FGF9^{Eks}$ were determined by sedimentation equilibrium centrifugation using the purified recombinant proteins (**Fig. 3a,b**). The estimated average molecular masses of $FGF9^{WT}$ and $FGF9^{Eks}$ were 39,264 and 32,929 Da, respectively, whereas the calculated monomeric molecular masses were 20,090 and 20,077 Da, respectively. These data suggest that $FGF9^{WT}$ primarily exists as a dimer, whereas $FGF9^{Eks}$ exists in a monomer–dimer equilibrium. The calculated association constants of $FGF9^{WT}$ and $FGF9^{Eks}$ were 10.4 μM^{-1} and 0.119 μM^{-1}, respectively. We further measured the sedimentation coefficient of $FGF9^{Eks}$ by sedimentation velocity centrifugation. The overlay plots of c(s)-sedimentation coefficient distributions show that $FGF9^{WT}$ has a unimodal peak at 3.0 S for a single ideal species, whereas $FGF9^{Eks}$ has bimodal peaks (2.2 S and 3.1 S) for two ideal species (**Fig. 3c,d**). This observation suggests that $FGF9^{WT}$ is present primarily as a dimer, whereas $FGF9^{Eks}$ exists primarily as a monomer. These interpretations are consistent with the retarded elution of $FGF9^{Eks}$

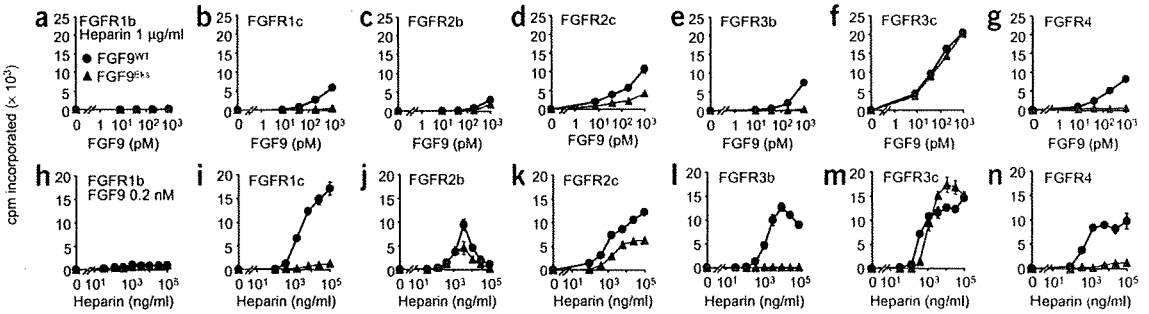

Figure 4 The *Eks* mutation affects the mitogenic activity of FGF9. **(a–g)** Dose-dependent changes in mitogenic activity of $FGF9^{WT}$ and $FGF9^{Eks}$. BaF3 cells expressing exogenous FGFR1b, 1c, 2b, 2c, 3b, 3c or 4 were treated with increasing concentrations of $FGF9^{WT}$ or $FGF9^{Eks}$ in the presence of 1 μg/ml heparin. Cell proliferation was determined by [^{3}H]thymidine incorporation after 36 h in culture. **(h–n)** Heparin-dependent changes in mitogenic activity of $FGF9^{WT}$ and $FGF9^{Eks}$. BaF3 cells expressing the respective FGFR were treated with increasing concentrations of heparin in the presence of 0.2 nM $FGF9^{WT}$ or $FGF9^{Eks}$. Cell proliferation was determined as above. Data are represented as mean ± s.e.m. of triplicate assays. These results are representative of at least two independent experiments.

relative to $FGF9^{WT}$ on a gel filtration column (**Fig. 3e**). Therefore, $FGF9^{Eks}$ is defective in homodimer formation.

$FGF9^{Eks}$ mediates less potent signaling via several FGFRs

To examine whether the *Eks* mutaion altered the binding of FGF9 to FGFRs by impairing the autoinhibitory mechanisms, we compared the ability of $FGF9^{WT}$ and $FGF9^{Eks}$ to activate FGFRs by assaying the mitogenic activity of both proteins on BaF3 cells expressing individual FGF receptors[17]. FGFR-expressing BaF3 cell lines were treated with increasing concentrations of purified recombinant FGF9 in the presence of 1 μg/ml heparin. Compared to $FGF9^{WT}$, $FGF9^{Eks}$ showed less activity on cells expressing any of the FGFRs except FGFR3c, where $FGF9^{Eks}$ showed equivalent activity (**Fig. 4a–g**). To test the ability of heparin to enhance FGF9 activity, we treated the BaF3 cell lines with increasing concentrations of heparin in the presence of 0.2 nM $FGF9^{WT}$ or $FGF9^{Eks}$. $FGF9^{Eks}$ also showed a decreased heparin-dependent mitotic response on all FGFRs except FGFR3c, where $FGF9^{Eks}$ showed higher activity in the presence of high concentrations of heparin (**Fig. 4h–n**). Because $FGF9^{Eks}$ does not mediate excess signaling via FGFRs, other properties of the altered protein must be responsible for the phenotype of the *Eks* mice.

The *Eks* mutation lowers FGF9 affinity for heparin

The decreased heparin-dependent mitogenic activity of $FGF9^{Eks}$ suggested that its affinity for heparin may be reduced. Heparin is functionally very similar to heparan sulfate, which is present in most tissues in the form of HSPGs. HSPGs function to modulate FGFR activation directly, by mediating FGF–FGFR interactions, and indirectly, by binding FGF ligands and regulating their diffusion through the extracellular matrix and thus their access to distant FGFRs[1,12,13,26]. As the gain-of-function property of $FGF9^{Eks}$ may not involve direct interaction with the FGFRs, we hypothesized that its decreased affinity for heparin might allow increased diffusion and thus bioavailability in

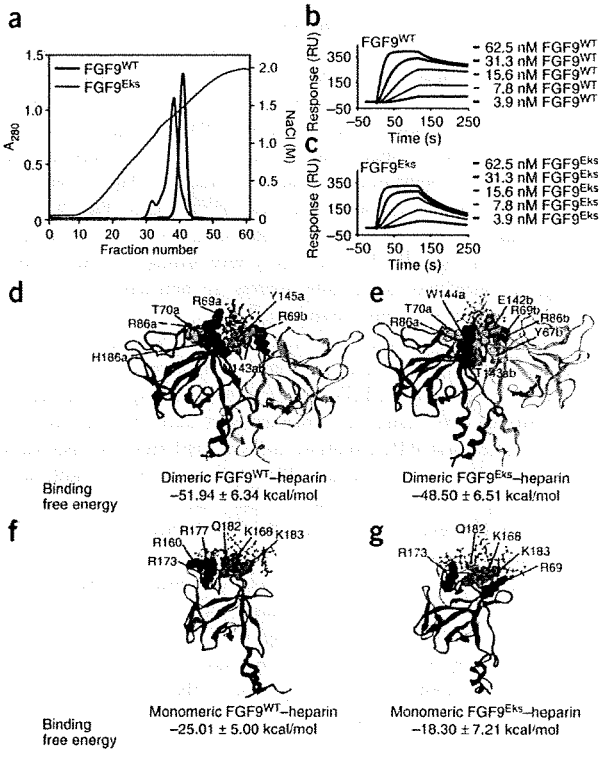

Figure 5 The *Eks* mutation reduces FGF9 affinity for heparin by impairing its dimerization. **(a)** Chromatographic analysis of the affinities of $FGF9^{WT}$ and $FGF9^{Eks}$ for heparin. $FGF9^{WT}$ or $FGF9^{Eks}$ were loaded onto a heparin-conjugated agarose column and eluted with a linear gradient of NaCl from 120 mM to 2.0 M (black line). Elution profiles of $FGF9^{WT}$ and $FGF9^{Eks}$ were determined by monitoring absorbance at 280 nm. **(b,c)** Surface plasmon resonance analysis of the affinities of $FGF9^{WT}$ and $FGF9^{Eks}$ for heparin. Sensorgrams indicating the interaction of $FGF9^{WT}$ **(b)** and $FGF9^{Eks}$ **(c)** with immobilized heparin were determined at different concentrations. The biosensor chip response is indicated on the *y* axis (RU) as a function of time (*x* axis) at room temperature. **(d–g)** The most probable solution structures of dimeric $FGF9^{WT}$–heparin **(d)**, dimeric $FGF9^{Eks}$–heparin **(e)**, monomeric $FGF9^{WT}$–heparin **(f)** and monomeric $FGF9^{Eks}$–heparin **(g)** complexes deduced by molecular-dynamics simulations. Heparin and protein residues that form important hydrogen bonds are drawn in ball and stick and space-filling modes. The single-letter amino acid code, residue number and chain code are indicated for each of these residues. Computed binding free energy of each complex is shown under the respective illustrated structure. Data are represented as mean ± s.d. of energies obtained from 200 molecular-dynamics snapshots in respective molecular-dynamics trajectory.

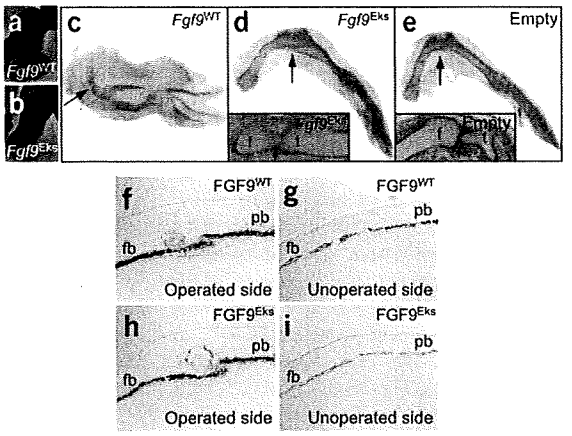

Figure 6 FGF9^{Eks} can inhibit joint and suture development as well as FGF9^{WT}. (**a–e**) Inhibition of knee joint development induced by ectopic expression of *Fgf9*^{WT} and *Fgf9*^{Eks}. Hindlimb buds of Hamburger-Hamilton stage 17 chickens were infected with RCAS-*Fgf9*^{WT}, RCAS-*Fgf9*^{Eks} or empty RCAS virus. (**a,b**) *Fgf9* expression was examined by *in situ* hybridization 2 d after infection. (**c–e**) Respective knee joints (arrows) were examined by Alcian blue staining and hematoxylin and eosin staining of sections through the knee joint (insets in **d** and **e**) 5 d after infection. f, femur; t, tibia. (**f–i**) Inhibition of coronal suture development by the ectopic presence of FGF9^{WT} and FGF9^{Eks}. FGF9^{WT} or FGF9^{Eks} beads were implanted onto the coronal suture in E15 mice, and the *Spp1* expression was examined by *in situ* hybridization 24 h after implantation. On the operated sides with FGF9^{WT} (**f**) and FGF9^{Eks} (**h**) bead implants, there was overlap of *Spp1* expression in the frontal and parietal bones, which was not seen on the unoperated sides (**g,i**). fb, frontal bone; pb, parietal bone.

tissues. To address this possibility, we first measured FGF9–heparin affinity by heparin affinity chromatography (**Fig. 5a**). FGF9^{WT} was eluted from heparin-conjugated agarose with 1.50 M NaCl as a single peak. In contrast, most FGF9^{Eks} was eluted at 1.38 M NaCl and a small fraction eluted at 1.10 M NaCl.

We next measured the kinetic constants for the FGF9^{Eks}–heparin interaction using surface plasmon resonance analysis (**Fig. 5b,c** and **Supplementary Table 1** online). The resulting sensorgrams were used for kinetic parameter determination by globally fitting the experimental data to a 1:1 interaction model. The association rate constant (k_a) of FGF9^{Eks} was slightly greater than that of FGF9^{WT}, whereas the dissociation rate constant (k_d) of FGF9^{Eks} was 18-fold greater than that of FGF9^{WT}. The dissociation constants (K_D) for FGF9^{WT} and FGF9^{Eks} were 0.71 ± 0.02 nM and 5.24 ± 0.03 nM, respectively, representing an 86% decrease in affinity of the FGF9^{Eks} protein for heparin.

Dimerization of FGF9 confers heparin affinity

The above studies indicate the *Fgf9*^{Eks} mutation concurrently affects monomer–dimer equilibrium and affinity for heparin. We thus went on to address whether the N143T substitution directly affects the affinity of FGF9 for heparin or whether it directly affects homodimerization and secondarily affects heparin affinity. However, direct biochemical measurements of the affinity of the two species for heparin are not possible because monomeric and dimeric forms of FGF9 are in equilibrium. We therefore analyzed the configuration of heparin-binding domains in monomeric and dimeric FGF9 using molecular-dynamics simulations and calculated the binding free energy between FGF9 and heparin using the molecular mechanics Poisson-Boltzmann/surface area (MM-PBSA) method. It is well known that the binding free energies calculated by this method show good qualitative but not quantitative agreement with experimental observations[27].

To model the heparin binding affinity of FGF9, we carried out molecular-dynamics simulations of 2:2 FGF9^{WT}–heparin and 2:2 FGF9^{Eks}–heparin complexes based on a 2:2:2 FGF2-FGFR1-heparin crystal structure (Protein Data Bank (PDB) ID: 1FQ9)[28]. The conformations of two heparin oligosaccharides in each complex were influenced by strong electrostatic repulsions, resulting in the exclusion of one heparin oligosaccharide from the complex (data not shown). This analysis suggested that 2:2 FGF9–heparin complexes would be unstable. In contrast, molecular-dynamics simulations of 2:1 FGF9^{WT}–heparin, 2:1 FGF9^{Eks}–heparin, 1:1 FGF9^{WT}–heparin and 1:1 FGF9^{Eks}–heparin complexes suggested that these complexes are stable (**Fig. 5d–g**). Molecular-dynamics simulations of dimeric FGF9–heparin complexes did not show a big difference in heparin-binding free energies for 2:1 FGF9^{WT}–heparin (dimeric FGF9^{WT}–heparin) and 2:1 FGF9^{Eks}–heparin (dimeric FGF9^{Eks}–heparin) complexes (**Fig. 5d,e**). This is due to the strong interaction between the negatively charged heparin oligosaccharide chain and the array of basic amino acid residues located in the heparin binding site near the groove of the dimer interface in both dimeric complexes. In addition, flexibility of the heparin oligosaccharide chain would help to maintain electrostatic interactions. Similarly, there was little difference in the heparin-binding free energies in 1:1 FGF9^{WT}–heparin (monomeric FGF9^{WT}–heparin) and 1:1 FGF9^{Eks}–heparin (monomeric FGF9^{Eks}–heparin) complexes (**Fig. 5f,g**). This is also due to heparin oligosaccharide chain flexibility, the strong negative charge of the heparin oligosaccharide and the presence of several basic amino acid residues in the heparin binding site. Therefore, the *Eks* mutation does not seem to influence the heparin binding affinity of either the dimeric or the monomeric FGF9–heparin complex. Because the heparin-binding free energies for dimeric FGF9 (**Fig. 5d,e**) were smaller than those for monomeric FGF9–heparin for both FGF9^{WT} and FGF9^{Eks} (**Fig. 5f,g**), the reduced binding affinity to heparin of the FGF9^{Eks} protein is most likely due to the shift in the monomer–dimer equilibrium toward the monomer. In summary, the *Eks* mutation primarily affects homodimerization of FGF9 and only secondarily affects heparin affinity.

FGF9^{Eks} is potentially hyperdiffusible in tissues

Heparin–FGF2 interactions have previously been shown to regulate the diffusibility of FGF2 (refs. 26,29). We hypothesized that the diffusibility of FGF9^{Eks} in tissues would be increased because of its lower affinity for heparin, leading to ectopic localization outside of the normal signaling domain and, consequently, ectopic activation of FGFRs. However, this model can only be considered if the following two prerequisites are met: first, *Fgf9* and *Fgfrs* are expressed in the proximity of the prospective elbow and knee joints and coronal sutures and, second, the increased diffusibility of FGF9^{Eks} is dominant over its decreased ability to activate FGFRs.

We first examined the expression of *Fgf9* and *Fgfr1*, *Fgfr2* and *Fgfr3* in the forelimb buds in E10.5 and E11.5 mice. *Fgf9* was expressed in migrating myoblasts, both in *Fgf9*$^{+/+}$ and *Fgf9*$^{Eks/Eks}$ mice (**Supplementary Fig. 3a,b,i,j** online). At E10.5, *Fgfr1*, *Fgfr2* and *Fgfr3* were expressed diffusely in the limb bud mesenchyme, overlapping the expression domain of *Col2a1* in both *Fgf9*$^{+/+}$ and *Fgf9*$^{Eks/Eks}$ tissues (**Supplementary Fig. 3c–h**). At E11.5, *Fgfr1* expression was excluded from the cartilaginous condensation, whereas *Fgfr2* and *Fgfr3*

expression was observed mainly in this location (**Supplementary Fig. 3k–p**). Therefore, mesenchymal cells in the prospective elbow joint express FGFRs.

Previous reports showed that *Fgf9* is expressed in the developing frontal and parietal bones, particularly strongly at the rims of the bones[18]. *Fgfr1*, *Fgfr2* and *Fgfr3* are expressed within and around the developing frontal and parietal bone domains[30]. Thus, the first prerequisite was validated.

FGF9^{Eks} is able to inhibit joint and suture development

To address the second prerequisite for our model, we examined the inhibitory effects of FGF9^{WT} and FGF9^{Eks} on joint development by ectopically expressing them in the chicken limb bud using a replication component retroviral vector (RCAS) transduction. RCAS-*Fgf9*^{WT}, RCAS-*Fgf9*^{Eks} or empty RCAS virus was used to infect the prospective hindlimb bud region in the lateral plate mesoderm. FGF9^{WT} and FGF9^{Eks} were expressed throughout the hindlimb buds (**Fig. 6a,b**). Ectopic expression of both *Fgf9*^{WT} and *Fgf9*^{Eks} caused knee joint fusion (**Fig. 6c,d**), whereas no abnormalities were induced by the empty vector (**Fig. 6e**). Therefore, FGF9^{Eks} retains inhibitory effects on joint development as well as FGF9^{WT}. It is notable that skeletal defects induced by the expression of FGF9^{WT} were widespread, whereas those mediated by FGF9^{Eks} were limited to the prospective joint regions. This is consistent with our finding that FGF9^{Eks} preferentially activates FGFR3c (**Fig. 4**), which is expressed in the bone anlagen (**Supplementary Fig. 3**), whereas FGF9^{WT} is expected to activate all of the mesodermally expressed FGFRs.

To examine the inhibitory effects of FGF9^{WT} and FGF9^{Eks} on suture development, we implanted FGF9-soaked AffiGel-Blue beads in the coronal suture of normal mouse fetal skulls around the initiation stage of the suture defect, at E15, by *ex utero* surgery. We first confirmed that approximately equal amounts of FGF9^{WT} and FGF9^{Eks} were loaded in each AffiGel-Blue bead and that the diffusion rates of FGF9^{WT} and FGF9^{Eks} from the beads were almost identical (**Supplementary Fig. 4** online). The expression of *Spp1*, an early osteoblast differentiation marker upregulated by FGF9, was examined 24 h after *in utero* bead placement. Grafts of FGF9^{WT} and FGF9^{Eks} beads also promoted ectopic *Spp1* expression at the leading edges of the frontal and parietal bones (**Fig. 6f–i**). This FGF9-induced ectopic expression of *Spp1* resembled that observed in the *Fgf9*$^{Eks/Eks}$ coronal suture (**Fig. 2m**, right). Therefore, ectopic expression of either FGF9^{Eks} or FGF9^{WT} within the suture inhibits suture development.

FGF9^{Eks} is more diffusible than FGF9^{WT} in developing tissues

To examine whether the diffusibility of FGF9^{Eks} in mesenchymal tissue is increased in comparison with FGF9^{WT}, we measured the diffusibility of FGF9^{WT} and FGF9^{Eks} in the skull following bead implantation (**Fig. 7a–e**). Because FGF9 upregulates *Spp1* expression, we could measure the area of high *Spp1* expression as an indication of

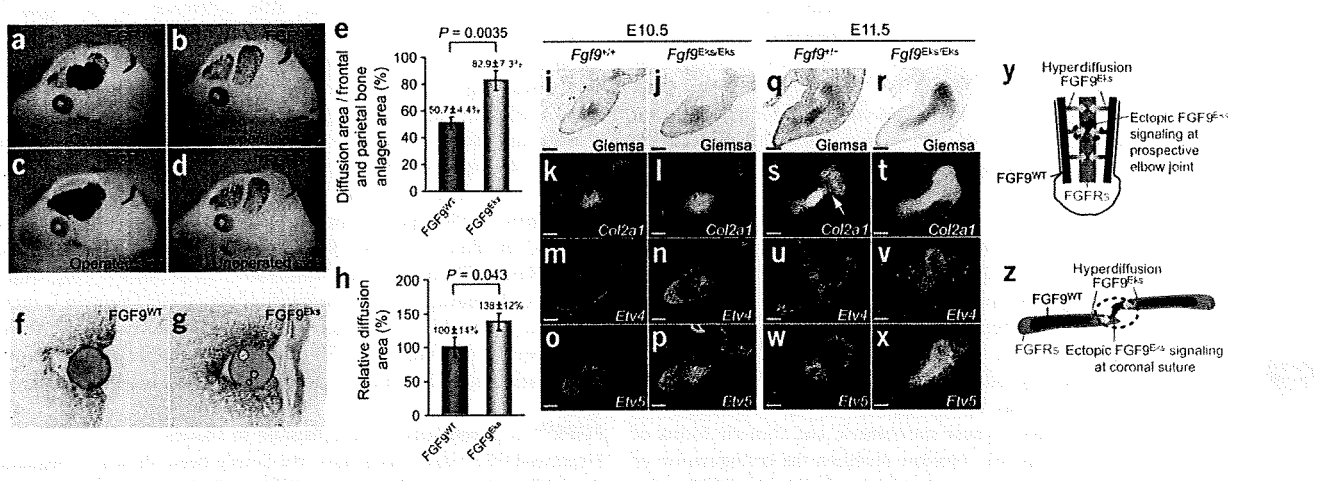

Figure 7 Ectopic FGF9^{Eks} signaling due to its hyperdiffusibility. **(a–e)** Increased diffusibility of FGF9^{Eks} in the skull bone anlagen. FGF9^{WT} or FGF9^{Eks} beads were implanted onto the coronal suture at E15 mice and *Spp1* expression was examined by whole-mount *in situ* hybridization 24 h after implantation. On the operated sides with FGF9^{WT} **(a)** and FGF9^{Eks} **(c)** bead implants, we observed well-defined intense signals in the frontal and parietal bone anlagen around the implants, which were not seen on the unoperated side **(b,d)**. This domain with intense *Spp1* signals reflects diffusibility of exogenous FGF9 proteins. We therefore compared diffusibility of FGF9^{WT} and FGF9^{Eks} based on the induced expression domain of *Spp1* **(e)**. The diffusion areas (%) in the frontal and parietal bone anlagen area were estimated from the area ratio of the intense *Spp1* expression against the frontal and parietal bone anlagen. Data are represented as mean ± s.e.m. of six operations. FGF9^{Eks} is more diffusible than FGF9^{WT}. Significance was determined by two-tailed Student's *t*-test. **(f–h)** Increased diffusibility of FGF9^{Eks} in the forelimb bud. FGF9^{WT} or FGF9^{Eks} beads were implanted into forelimb buds of *Fgf9*$^{-/-}$ embryos of E10.5 mice. Diffusion of exogenous FGF9^{WT} **(f)** and FGF9^{Eks} **(g)** after 2 h was immunodetected using a FGF9 antibody. **(h)** The diffusion area of FGF9^{Eks} and FGF9^{WT} was measured at the level of the equator of the beads. Data are represented as mean (FGF9^{WT} = 100%) ± s.e.m. of four (FGF9^{WT}) or five (FGF9^{Eks}) operations. FGF9^{Eks} is also more diffusible than FGF9^{WT} in limb buds. Significance was determined by one-tailed Student's *t*-test. **(i–x)** The downstream target genes of FGF signaling, *Etv4* and *Etv5*, are expressed ectopically in the prospective elbow joint in *Fgf9*$^{Eks/Eks}$ mice. Counterstaining with Giemsa **(i,j,q,r)** and *in situ* detection of *Col2a1* **(k,l,s,t)**, *Etv4* **(m,n,u,v)** and *Etv5* **(o,p,w,x)** in the forelimb buds of *Fgf9*$^{+/+}$ and *Fgf9*$^{Eks/Eks}$ embryos at E10.5 and E11.5. There was ectopic expression of *Etv4* **(n,v)** and *Etv5* **(p,x)**, in the cartilaginous condensation including the prospective elbow joint position, which was demarcated as the gap of *Col2a1* expression **(s**, arrow**)**, in *Fgf9*$^{Eks/Eks}$, which were not seen in *Fgf9*$^{+/+}$ mice **(m,o,u,w)**. Scale bars, 100 μm. **(y)** A model for the pathogenic mechanism underlying elbow joint synosotsis in *Fgf9*$^{Eks/Eks}$ mice. In *Fgf9*$^{Eks/Eks}$ mice, ectopic FGF9 signaling due to hyperdiffusion of FGF9^{Eks} at the prospective elbow joint may inhibit the initiation of joint development. **(z)** A model for the pathogenic mechanism underlying premature fusion of the coronal suture in *Fgf9*$^{Eks/Eks}$ mice. In *Fgf9*$^{Eks/Eks}$ mice, ectopic FGF9 signaling due to hyperdiffusion of FGF9^{Eks} at the coronal suture may promote ectopic osteogenesis and subsequently induce premature fusion of the suture.

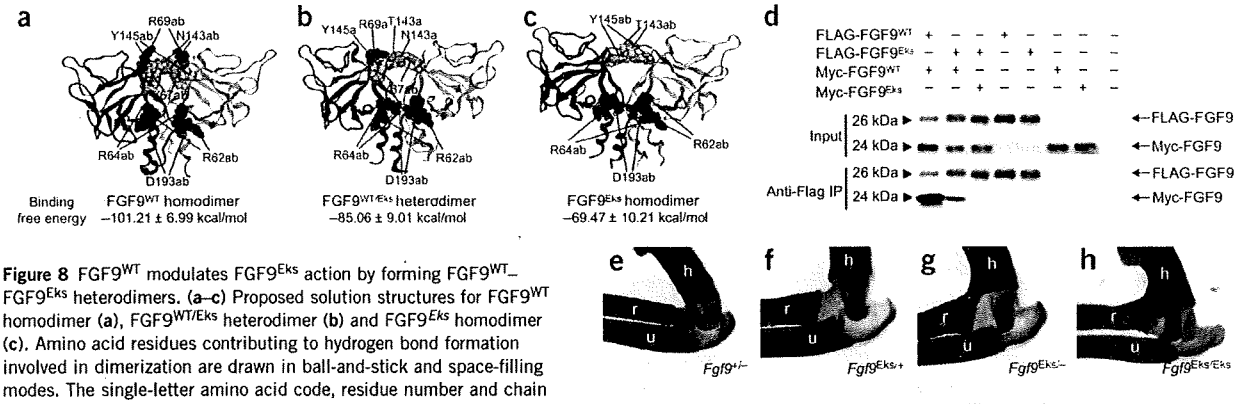

Figure 8 FGF9^{WT} modulates FGF9^{Eks} action by forming FGF9^{WT}–FGF9^{Eks} heterodimers. (**a–c**) Proposed solution structures for FGF9^{WT} homodimer (**a**), FGF9$^{WT/Eks}$ heterodimer (**b**) and FGF9^{Eks} homodimer (**c**). Amino acid residues contributing to hydrogen bond formation involved in dimerization are drawn in ball-and-stick and space-filling modes. The single-letter amino acid code, residue number and chain code are indicated for each of these residues. Computed binding free energy of each dimer is shown under the respective illustrated structure. Data are represented as mean ± s.d. of energies obtained from 200 molecular-dynamics snapshots in respective molecular-dynamics trajectory. (**d**) FGF9^{WT} is capable of forming dimers with FGF9^{Eks}. The expression of FGF9^{WT} homodimers, FGF9$^{WT/Eks}$ heterodimers and FGF9^{Eks} homodimers was analyzed using immunoprecipitation and protein blots. The expression vectors for FLAG- or Myc-tagged FGF9^{WT} and FGF9^{Eks} were transfected into COS7 cells and culture supernatants were subjected to immunoprecipitation and protein blot analysis. (**e–h**) Less severe elbow joint synostosis in *Fgf9*$^{Eks/+}$ than *Fgf9*$^{Eks/-}$. Forelimbs from *Fgf9*$^{+/-}$, *Fgf9*$^{Eks/+}$, *Fgf9*$^{Eks/-}$ and *Fgf9*$^{Eks/Eks}$ embryos at E17.5 were stained with Alcian blue and Alizarin red. Synostotic change is restricted to the cartilaginous component in *Fgf9*$^{Eks/+}$ embryos, whereas it is extended to the bony component in *Fgf9*$^{Eks/-}$ and *Fgf9*$^{Eks/Eks}$ embryos. h, humerus; r, radius; u, ulna.

the distance over which FGF9 exerts its effects. Implantation of FGF9^{Eks} beads resulted in a larger area of *Spp1* expression (high *Spp1* expression area / Frontal and parietal bone anlagen area = 82.9 ± 7.3%) (± s.e.m.) compared with beads loaded with FGF9^{WT} (50.7 ± 4.4%; $P = 0.0035$), suggesting that the altered protein diffused more effectively through the developing tissue.

Next, we investigated the diffusibility of FGF9^{Eks} in forelimb buds. FGF9^{WT}- or FGF9^{Eks}-soaked AffiGel-Blue beads were grafted into the dorsal and central forelimb bud region of *Fgf9*$^{-/-}$ embryos around the initiation stage of the joint defect, at E10.5. FGF9 protein released from the beads into mesenchymal tissue 2 h after implantation was detected by immunohistochemistry using FGF9 antibodies on sections (**Fig. 7f–h**). This analysis showed that FGF9^{Eks} permeated through the limb bud mesenchyme to a greater extent (relative disffusion area = 138 ± 12%) (± s.e.m.) than FGF9^{WT} (100 ± 14%; $P = 0.043$), supporting the hypothesis that FGF9^{Eks} is more diffusible than FGF9^{WT}.

Ectopic FGF signaling in the prospective joint of *Eks* mice

To examine whether diffusion of endogenous FGF9^{Eks} is increased in comparison to FGF9^{WT}, we determined the degree of activation of FGFRs in the prospective elbow joint of *Fgf9*$^{Eks/Eks}$ mice. As a readout for FGFR signaling, we examined the expression of *Etv4* and *Etv5*, both of which are known to be transcriptionally activated by FGF signaling, in the forelimb buds[31] (**Fig. 7i–x**). In wild-type E10.5 limbs, we did not observe the intensive expression of *Etv4* or *Etv5* within the region undergoing cartilaginous condensation demarcated by *Col2a1* expression (**Fig. 7m,o**). However, in E10.5 *Fgf9*$^{Eks/Eks}$ limbs, we found ectopic expression of both *Etv4* and *Etv5* in the cartilaginous condensation (**Fig. 7n,p**). At E11.5, *Etv4* and *Etv5* were expressed in the myoblasts and cells surrounding the cartilaginous condensation in wild-type mice (**Fig. 7u,w**), whereas in *Fgf9*$^{Eks/Eks}$ mice, we observed clear expression of *Etv4* and *Etv5* in the cartilaginous condensation including the prospective elbow joint position (**Fig. 7v,x**). These results demonstrate ectopic FGF signaling in the prospective elbow joint in *Fgf9*$^{Eks/Eks}$ mice. Because the ectopic expression domain of *Etv4* and *Etv5* in *Fgf9*$^{Eks/Eks}$ mice was not consistent with the *Fgf9* expression domain (**Supplementary Fig. 3a,b,i,j**), this outcome is likely due to increased diffusion of FGF9^{Eks} protein over a larger area than FGF9^{WT}.

From these results, we propose a mechanism of elbow joint synostosis in *Fgf9*$^{Eks/Eks}$ mice in which FGF9^{Eks} produced by myoblasts diffuses beyond its normal range and ectopically activates FGFRs in the prospective elbow joint, preventing joint formation (**Fig. 7y**). Similarly, FGF9^{Eks} produced at the rims of the frontal and parietal bones diffuses beyond its normal area and ectopically activates FGFRs in the coronal suture mesenchyme, promoting the fusion of coronal sutures (**Fig. 7z**).

Genetic validation of the hyperdiffusible model

A prediction of our model is that the severity of synostotic phenotypes will correlate with a shift in the equilibrium of FGF9 from dimer toward monomer. By molecular-dynamics simulations, we estimated that FGF9^{WT} homodimer, FGF9$^{WT/Eks}$ heterodimer and FGF9^{Eks} homodimer have ten, eight, six intermonomer hydrogen bonds, respectively (**Fig. 8a–c** and **Supplementary Table 2** online). From these results, we calculated the binding free energy of the FGF9$^{WT/Eks}$ heterodimer to be between those of the FGF9^{WT} and FGF9^{Eks} homodimers (**Fig. 8a–c**), suggesting that FGF9$^{WT/Eks}$ heterodimers are more stable than FGF9^{Eks} homodimers. If our model is correct, FGF9^{WT} should interfere with FGF9^{Eks} action by forming FGF9$^{WT/Eks}$ heterodimers. In other words, skeletal phenotypes due to the *Eks* mutation should be alleviated by the expression of FGF9^{WT}.

We first sought experimental evidence that the FGF9$^{WT/Eks}$ heterodimer was substantially more stable than the FGF9^{Eks} homodimer. We addressed this issue by immunoprecipitation and protein blot analysis after tagging FGF9^{WT} and FGF9^{Eks} with Flag or Myc peptides. Flag-FGF9^{WT} or Flag-FGF9^{Eks} was overexpressed together with Myc-FGF9^{WT} or Myc-FGF9^{Eks} in COS7 cells and the culture supernatants were subjected to the immunoprecipitation and protein blot analysis (**Fig. 8d**). We readily detected Flag-FGF9^{WT}–Myc-FGF9^{WT} dimers. Flag-FGF9^{Eks}–Myc-FGF9^{WT} dimers were detected at lower level; however, Flag-FGF9^{Eks}–Myc-FGF9^{Eks}

dimers did not form under these conditions. These data suggest that $FGF9^{WT}$ and $FGF9^{Eks}$ can form heterodimers that are more stable than $FGF9^{Eks}$ homodimers.

We finally examined whether the elbow synostosis caused by $FGF9^{Eks}$ could be alleviated by the expression of $FGF9^{WT}$. We thus compared the severity of elbow synostosis in $Fgf9^{Eks/+}$ and compound heterozygous mutants ($Fgf9^{Eks/-}$) relative to that of $Fgf9^{+/-}$ and $Fgf9^{Eks/Eks}$ mice (**Fig. 8e–h**). Elbow joint formation was not affected in $Fgf9^{+/-}$ mice (**Fig. 8e**), whereas elbow synostosis in $Fgf9^{Eks/Eks}$ mice involved both cartilaginous and bony components (**Fig. 8h**). In contrast, the synostosis in $Fgf9^{Eks/+}$ mice was limited to the cartilaginous component (**Fig. 8f**), whereas the involvement of the bony component in $Fgf9^{Eks/-}$ mice was similar to that of $Fgf9^{Eks/Eks}$ mice (**Fig. 8g**). Therefore, elbow synostosis in $Fgf9^{Eks/-}$ is more severe than in $Fgf9^{Eks/+}$. These findings strongly support our model that the monomer–dimer status of FGF9 influences its affinity for HSPGs and, consequently, its distribution in developing tissues.

DISCUSSION

In the present study, we identified a missense mutation in the *Fgf9* gene that is responsible for the *Eks* mutant phenotype, which includes elbow and knee joint synostosis and craniosynostosis. We further demonstrate that the N143T substitution in FGF9 favors formation of the monomeric form of FGF9, which binds to heparin with a lower affinity than dimeric FGF9. The decreased affinity for heparin leads to increased diffusion of the altered protein in developing tissues, resulting in ectopic FGF9 signaling. We propose that regulation of the monomer–dimer equilibrium of FGF9, and potentially of other FGFs, and its affinity for HSPGs is a mechanism that functions to shape FGF9 concentration gradients in developing tissues. We further propose that these biochemical properties of FGF9 restrict its signaling activity to limited skeletal domains. Data presented here and in previous studies indicate that low FGF signaling in the presumptive joint space is necessary for the formation of the joint space and maintenance of an open suture[20,21]. Common usage of receptor binding and homodimerization sites of FGF9 could be at least in part instrumental for local modulation of FGF9 signaling activity.

Homodimerization is suggested to be a common feature of the FGF9/16/20 subfamily[32] and of FGF2 (refs. 33,34). It is not known to what extent homodimerization affects the activity of other FGFs. The discovery that a mutation in *Fgf9* can affect homodimerization, affinity for heparin and biological activity suggests that pharmacological agents that affect FGF homodimerization could be useful tools to modulate its activity.

METHODS

Detection of a mutation in the *Fgf9* gene. To identify the mutation responsible for the *Eks* mutant phenotype, we surveyed the cDNA sequence of *Fgf9* from normal (+/+), heterozygous (*Eks*/+) and homozygous (*Eks*/*Eks*) mice through reverse transcription-PCR (RT-PCR) and direct sequencing of RT-PCR products.

For genotyping of the *Eks* allele, genomic DNA spanning the *Eks* mutation was amplified by PCR using specific primers (**Supplementary Table 3** online). PCR products were digested with the diagnostic *Bsr*I restriction enzyme. Wild-type mice show two bands of 147 bp and 42 bp, whereas the *Eks* allele shows one band of 189 bp (**Supplementary Fig. 5** online).

Skeletal and histological preparations. Bones and cartilage of E17.5 fetuses were stained with Alizarin red and Alcian blue as previously described[35]. For histological preparations, tissues were fixed in 4% paraformaldehyde, embedded in paraffin, sectioned at 5 μm, and stained with hematoxylin and eosin and von Kossa.

***In situ* hybridization.** *In situ* hybridization of paraffin sections was done as previously described[36], using radiolabeled antisense RNA for *Gdf5* (MGI: 95688), *Col2a1* (MGI: 88452), *Spp1* (MGI: 98389), *Runx2* (MGI: 99829), *Fgf9* (MGI: 104723), *Fgfr1* (MGI: 95522), *Fgfr2* (MGI: 95523), *Fgfr3* (MGI: 95524), *Etv4* (MGI: 99423) and *Etv5* (MGI: 1096867). *In situ* hybridization after bead implantation in fetal skulls was done as previously described[24].

$FGF9^{WT}$ and $FGF9^{Eks}$ expression and purification. $FGF9^{WT}$ and $FGF9^{Eks}$ expression and purification were done as described in **Supplementary Methods**.

Analytical ultracentrifugation. All analytical ultracentrifuge experiments were done on a Beckman Coulter XL-I analytical ultracentrifuge. We diluted the samples in 25 mM ammonium acetate buffer (pH 5.5) containing 120 mM NaCl. The partial specific volumes were estimated as 0.7317 ml/g ($FGF9^{WT}$) or 0.7322 ml/g ($FGF9^{Eks}$) by SEDNTERP software. All experiments were done at 20 °C and the absorbance wavelength was 280 nm. We carried out sedimentation equilibrium experiments with six channel centerpieces, with loading concentrations of 0.8, 0.4 and 0.2 mg/ml. Data were obtained at 12, 14 and 16 k rpm for $FGF9^{WT}$ or at 14, 16 and 18 k rpm for $FGF9^{Eks}$. A total equilibration time of 16 h was used for each speed with scans taken at 12, 14 and 16 h. We analyzed the sedimentation equilibrium data using the Beckman XL-A/XL-I Data Analysis software. All nine datasets (three speeds, three concentrations) were fitted together by 'self association model' calculation. Sedimentation velocity experiments were carried out with double sector centerpieces. Protein concentrations were 0.4, 0.3 or 0.2 mg/ml. We scanned the absorbance data 100 times every 5 min at 40 k rpm. The measurements data were analyzed by SEDFIT software.

Analytical gel filtration chromatography. Purified $FGF9^{WT}$ and $FGF9^{Eks}$ (100 μl of 2 mg/ml) were loaded onto a Superdex75 10/300 GL column (GE Healthcare) equilibrated with a 25 mM ammonium acetate buffer (pH 5.5) containing 120 mM NaCl. The samples were eluted with the same buffer.

Mitogenic assays. The ability of $FGF9^{WT}$ and $FGF9^{Eks}$ to transduce signals via FGFRs was analyzed by a mitogenic assay using BaF3 cells expressing specific FGFRs as described previously[17]. We plated 5,000 cells per well in a 96-well assay plate in media containing varying concentrations of FGF9 and heparin (Wako). $FGF9^{WT}$ or $FGF9^{Eks}$ were added to each well for a total volume of 200 μl per well. The cells were then incubated at 37 °C for 36 h. We added 1 μCi of [^{3}H]thymidine to each well in 20 μl of media. The cells were harvested after 4 h by filtration through glass fiber paper and the incorporated [^{3}H]thymidine was counted on a Wallac MicroBeta TriLux scintillation counter (PerkinElmer).

Analytical heparin affinity chromatography. We loaded 3 mg of purified $FGF9^{WT}$ and $FGF9^{Eks}$ onto a 1 ml HiTrap heparin HP column (GE Healthcare) equilibrated with 25 mM ammonium acetate buffer (pH 5.5) containing 120 mM NaCl. The bound $FGF9^{WT}$ or $FGF9^{Eks}$ were eluted with a linear gradient of NaCl (120 mM to 2.0 M) in the same buffer.

Surface plasmon resonance analysis of FGF9–heparin interactions. Surface plasmon resonance analysis for measurements of $FGF9^{WT}$–heparin and $FGF9^{Eks}$–heparin interactions were done using a BIAcore 3000 instrument (Biacore AB). In order to immobilize heparin (Wako) on the streptavidin-conjugated sensor chip SA, 100 μg/ml biotinylated heparin in HBS-EP buffer was injected at a flow rate of 10 μl/min and was immobilized to 63 response units (RU). All measurements were carried out at room temperature, and refractive index errors due to bulk solvent effects were corrected by subtracting responses on the noncoated sensor chip for the $FGF9^{WT}$ and $FGF9^{Eks}$ concentrations used. To obtain kinetic data, we injected different concentrations of analytes ($FGF9^{WT}$ and $FGF9^{Eks}$) in HBS-EP over the heparin sensor chip at a flow rate of 20 μl/min. At the end of each sample injection (120 s), HBS-EP buffer was passed over the sensor surface to monitor the dissociation phase. Following 120 s of dissociation, the sensor surface was regenerated by injection of 5 μl of 1 M NaCl in HBS-EP. We used five different analyte concentrations to determine the kinetic parameters for each interaction. Kinetic parameters were obtained by global fitting of the sensorgrams to a 1:1 model using BIAevaluation software.

Molecular-dynamics simulation. Starting structures of monomeric $FGF9^{WT}$, dimeric $FGF9^{WT}$, monomeric $FGF9^{WT}$-heparin, dimeric $FGF9^{WT}$-heparin and $FGF9^{Eks}$ for molecular-dynamics simulations were taken from the PDB (PDB ID: 1IHK)[14]. The structures of monomeric $FGF9^{Eks}$, dimeric $FGF9^{Eks}$ and heterodimeric $FGF9^{WT/Eks}$ were constructed based on $FGF9^{WT}$ using molecular modeling software MOE (Chemical Computing Group). A hexasasaccharide (UAP-SGN-IDU-SGN-IDU-SGN) is used as a heparin oligosaccharide. UAP is 1,4-dideoxy-5-dehydro-O2-sulfo-glucuronic acid, SGN is O6-disulfo-glucosamin and IDU is 1,4-dideoxy-O2-sulfo-glucuronic acid. For monomeric $FGF9^{WT}$–heparin and dimeric $FGF9^{WT}$–heparin simulations, heparin oligosaccharide was bound to $FGF9^{WT}$ structures obtained from molecular-dynamics simulations using the molecular docking program GOLD (version 3.0)[37]. In the docking protocol, the standard default setting of GA parameters was used and GoldScore was used as the scoring function. The structures of monomeric $FGF9^{Eks}$–heparin and dimeric $FGF9^{Eks}$–heparin were built in the same manner as $FGF9^{WT}$–heparin complexes. All the starting structures for molecular-dynamics simulations were surrounded by TIP3P water molecules[38] spherically. After energy minimizations, all molecular-dynamics simulations were carried out for 10 ns at 300 K using modified Amber 8.0 (ref. 39) for MDGRAPE3 system[40]. The Amber ff03 force field[41] was adopted, and the simulation time step was set at 1 s. We calculated the binding free energies by the molecular mechanics Poisson-Boltzmann/surface area (MM-PBSA) method[42] using the last 2 ns molecular-dynamics trajectories.

Retroviral misexpression. Mouse *Fgf9*^{WT} and *Fgf9*^{Eks} cDNAs were cloned into the RCASBP(A) vector[43]. The virus solutions were injected into the hind limb bud of chicken embryos at Hamburger-Hamilton stage 17. We examined the expression of mouse *Fgf9* transcripts and skeletal changes 2 and 5 d after injection, respectively.

Subcutaneous insertion of $FGF9^{Eks}$ beads in mouse fetal skulls. AffiGel-Blue beads (BioRad) soaked in 100 μg/ml $FGF9^{WT}$ or $FGF9^{Eks}$ were implanted onto E15 mouse skulls by *ex utero* surgery as previously described[24] Operated heads were collected 24 h later and *Spp1* transcripts were detected by whole-mount *in situ* hybridization. The area of *Spp1* expression was measured using NIH image software.

Implantation of $FGF9^{Eks}$ beads in mouse forelimb buds. AffiGel-Blue beads that had been soaked in 500 μg/ml $FGF9^{WT}$ or $FGF9^{Eks}$ were implanted into the dorsal and central region of E10.5 *Fgf9*$^{-/-}$ forelimb buds. Limb buds were subsequently cultured for 2 h on Transwell filters (Costar, Coaning) in serum-free medium (BGJb, 2 mg/ml BSA, penicillin (50 units/ml), streptomycin (50 μg/ml)), in a humid, 37 °C and 5% CO_2 environment. Explants were fixed in 4% paraformaldehyde and embedded in paraffin. Sections through the equator of the bead were analyzed for exogenous FGF9 using goat antibody to FGF9 (R&D Systems) and a cell and tissue staining kit HRP-AEC system (R&D Systems). We analyzed the signal area and intensity using NIH image software.

Immunoprecipitation and protein blot analysis. cDNA fragments encoding the full length mouse $FGF9^{WT}$ and $FGF9^{Eks}$ proteins were cloned into the p3xFlag-CMV-14 vector (Sigma-Aldrich) and into the pCMV-Tag3B vector (Stratagene) to allow expression of FGF9 proteins with either C-terminal Myc or 3xFlag tags. These vectors were transfected into COS7 cells, and 48 h later, culture supernatants were incubated with anti-Flag M2 affinity beads (Sigma-Aldrich) for 1 h at RT and washed three times with PBS and then subjected to protein blots with antibody to Flag M2 (Sigma-Aldrich) or antibody to Myc (Upstate).

Note: Supplementary information is available on the Nature Genetics website.

ACKNOWLEDGMENTS

This study was supported in part by the RIKEN Structural Genomics/Proteomics Initiative (RSGI) and the National Project on Protein Structural and Functional Analysis, Ministry of Education, Culture, Sports, Science and Technology of Japan (S.Y.) and US National Institutes of Health grant HD049808 (D.M.O.).

AUTHOR CONTRIBUTIONS

M.H., D.M.O. and H.K. developed the project and wrote the manuscript. M.H., S.H. and H.K. contributed to the purification of FGF9 proteins, mitogenic assays, analytical gel filtration chromatography, analytical heparin affinity chromatography, surface plasmon resonance analysis, skeletal preparation, histological analyses and *in situ* hybridization of sections, implantation of FGF9 beads in mouse forelimb buds and immunoprecipitation and protein blot analysis. H.M., A.O. and H.K. contributed to the identification of the *Eks* mutation. N.O., N.F. and M.T. contributed to the molecular-dynamics simulation. T.N. and S.I. contributed to the implantation of FGF9 beads in mouse fetal skulls. R.A., M.S. and S.Y. contributed to the analytical ultracentrifugation. Y.S. and A.K. contributed to the retroviral misexpression. Y.M.-K. contributed to the *in situ* hybridization of sections.

Published online at http://www.nature.com/naturegenetics/
Reprints and permissions information is available online at http://npg.nature.com/reprintsandpermissions/

1. Ornitz, D.M. & Itoh, N. Fibroblast growth factors. *Genome Biol.* **2**, reviews 3005 (2001).
2. Wilkie, A.O.M. Bad bone, absent smell, selfish testes: the pleiotropic consequences of human FGF receptor mutations. *Cytokine Growth Factor Rev.* **16**, 187–203 (2005).
3. Su, N., Du, X. & Chen, L. FGF signaling: its role in bone development and human skeleton diseases. *Front. Biosci.* **13**, 2842–2865 (2008).
4. Ornitz, D.M. & Marie, P.J. FGF signaling pathways in endochondral and intramembranous bone development and human genetic disease. *Genes Dev.* **16**, 1446–1465 (2002).
5. Martin, G.R. The roles of FGFs in the early development of vertebrate limbs. *Genes Dev.* **12**, 1571–1586 (1998).
6. Ornitz, D.M. FGF signaling in the developing endochondral skeleton. *Cytokine Growth Factor Rev.* **16**, 205–213 (2005).
7. Montero, A. *et al.* Disruption of the fibroblast growth factor-2 gene results in decreased bone mass and bone formation. *J. Clin. Invest.* **105**, 1085–1093 (2000).
8. Hung, I.H., Yu, K., Lavine, K.J. & Ornitz, D.M. FGF9 regulates early hypertrophic chondrocyte differentiation and skeketal vascularization in the developing stylopod. *Dev. Biol.* **307**, 300–313 (2007).
9. Liu, Z., Xu, J., Colvin, J.S. & Ornitz, D.M. Coordination of chondrogenesis and osteogenesis by fibroblast growth factor 18. *Genes Dev.* **16**, 859–869 (2002).
10. Ohbayashi, N. *et al.* FGF18 is required for normal cell proliferation and differentiation during osteogenesis and chondrogenesis. *Genes Dev.* **16**, 870–879 (2002).
11. Garofalo, S. *et al.* Skeletal dysplasia and defective chondrocyte differentiation by targeted overexpression of fibroblast growth factor 9 in transgenic mice. *J. Bone Miner. Res.* **14**, 1909–1915 (1999).
12. Ornitz, D.M. FGFs, heparan sulfate and FGFRs: complex interactions essential for development. *Bioessays* **22**, 108–112 (2000).
13. Nybakken, K. & Perrimon, N. Heparan sulfate proteoglycan modulation of developmental signaling in *Drosophila*. *Biochim. Biophys. Acta* **1573**, 280–291 (2002).
14. Plotnikov, A.N. *et al.* Crystal structure of fibroblast growth factor 9 reveals regions implicated in dimerization and autoinhibition. *J. Biol. Chem.* **276**, 4322–4329 (2001).
15. Hecht, H.J. *et al.* Structure of fibroblast growth factor 9 shows a symmetric dimer with unique receptor- and heparin-binding interfaces. *Acta Crystallogr. D Biol. Crystallogr.* **57**, 378–384 (2001).
16. Murakami, H. *et al.* Elbow knee synostosis (Eks): a new mutation on mouse Chromosome 14. *Mamm. Genome* **13**, 341–344 (2002).
17. Ornitz, D.M. *et al.* Receptor specificity of the fibroblast growth factor family. *J. Biol. Chem.* **271**, 15292–15297 (1996).
18. Hajihosseini, M.K. & Heath, J.K. Expression patterns of fibroblast growth factors-18 and -20 in mouse embryos is suggestive of novel roles in calvarial and limb development. *Mech. Dev.* **113**, 79–83 (2002).
19. Colvin, J.S., Feldman, B., Nadeau, J.H., Goldfarb, M. & Ornitz, D.M. Genomic organization and embryonic expression of the mouse fibroblast growth factor 9 gene. *Dev. Dyn.* **216**, 72–88 (1999).
20. Wang, Q., Green, R.P., Zhao, G. & Ornitz, D.M. Differential regulation of endochondral bone growth and joint development by FGFR1 and FGFR3 tyrosine kinase domains. *Development* **128**, 3867–3876 (2001).
21. Eswarakumar, V.P., Horowitz, M.C., Locklin, R., Morriss-Kay, G.M. & Lonai, P. A gain-of-function mutation of *Fgfr2c* demonstrates the roles of this receptor variant in osteogenesis. *Proc. Natl. Acad. Sci. USA* **101**, 12555–12560 (2004).
22. Storm, E.E. & Kingsley, D.M. Joint patterning defects caused by single and double mutations in members of the bone morphogenetic protein (BMP) family. *Development* **122**, 3969–3979 (1996).
23. Nalin, A.M., Greenlee, T.K. & Sandell, L.J. Collagen gene expression during development of avian synovial joints: Transient expression of types II and XI collagen genes in the joint capsule. *Dev. Dyn.* **203**, 352–362 (1995).
24. Iseki, S. *et al. Fgfr2* and *osteopontin* domains in the developing skull vault are mutually exclusive and can be altered by locally applied FGF2. *Development* **124**, 3375–3384 (1997).

25. Yoshida, T. *et al.* Twist is required for establishment of the mouse coronal suture. *J. Anat.* **206**, 437–444 (2005).
26. Flaumenhaft, R., Moscatelli, D. & Rifkin, D.B. Heparin and heparan sulfate increase the radius of diffusion and action of basic fibroblast growth factor. *J. Cell Biol.* **111**, 1651–1659 (1990).
27. Woo, H.J. & Roux, B. Calculation of absolute protein-ligand binding free energy from computer simulations. *Proc. Natl. Acad. Sci. USA* **102**, 6825–6830 (2005).
28. Schlessinger, J. *et al.* Crystal structure of a ternary FGF-FGFR-heparin complex reveals a dual role for heparin in FGFR binding and dimerization. *Mol. Cell* **6**, 743–750 (2000).
29. Dowd, C.J., Cooney, C.L. & Nugent, M.A. Heparan sulfate mediates bFGF transport through basement membrane by diffusion with rapid reversible binding. *J. Biol. Chem.* **274**, 5236–5244 (1999).
30. Johnson, D., Iseki, S., Wilkie, A.O.M. & Morriss-Kay, G.M. Expression patterns of Twist and *Fgfr1, -2* and *-3* in the developing mouse coronal suture suggest a key role for Twist in suture initiation and biogenesis. *Mech. Dev.* **91**, 341–345 (2000).
31. Tsang, M. & Dawid, I.B. Promotion and attenuation of FGF signaling through the Ras–MAPK pathway. *Sci. STKE* **2004**, pe17 (2004).
32. Mohammadi, M., Olsen, S.K. & Ibrahimi, O.A. Structural basis for fibroblast growth factor receptor activation. *Cytokine Growth Factor Rev.* **16**, 107–137 (2005).
33. Ornitz, D.M. *et al.* Heparin is required for cell-free binding of basic fibroblast growth factor to a soluble receptor and for mitogenesis in whole cells. *Mol. Cell. Biol.* **12**, 240–247 (1992).
34. Venkataraman, G., Shriver, Z., Davis, J.C. & Sasisekharan, R. Fibroblast growth factors 1 and 2 are distinct in oligomerization in the presence of heparin-like glycosaminoglycans. *Proc. Natl. Acad. Sci. USA* **96**, 1892–1897 (1999).
35. Kessel, M. & Gruss, P. Murine developmental control genes. *Science* **249**, 374–379 (1990).
36. Kessel, M. & Gruss, P. Homeotic transformations of murine vertebrae and concomitant alteration of Hox codes induced by retinoic acid. *Cell* **67**, 89–104 (1991).
37. Verdonk, M.L., Cole, J.C., Hartshorn, M.J., Murray, C.W. & Taylor, R.D. Improved protein-ligand docking using GOLD. *Proteins* **52**, 609–623 (2003).
38. Jorgensen, W.L., Chandrasekhar, J., Madura, J.D., Impey, R.W. & Klein, M.L. Comparison of simple potential functions for simulating liquid water. *J. Chem. Phys.* **79**, 926–935 (1983).
39. Case, D.A. *et al. AMBER 8* (University of California, San Francisco, 2004).
40. Narumi, T. *et al.* A 55 Tflops simulation of amyloid-forming peptides from yeast prion Sup35 with the special-purpose computer System MD-GRAPE3. <http://doi.acm.org/10.1145/1188455.1188506> (2006).
41. Duan, Y. *et al.* A point-charge force field for molecular mechanics simulations of proteins based on condensed-phase quantum mechanical calculations. *J. Comput. Chem.* **24**, 1999–2012 (2003).
42. Srinivasan, J., Miller, J., Kollma, P.A. & Case, D.A. Continuum solvent studies of the stability of RNA hairpin loops and helices. *J. Biomol. Struct. Dyn.* **16**, 671–682 (1998).
43. Hughes, S.H., Greenhouse, J.J., Petropoulos, C.J. & Sutrave, P. Adaptor plasmids simplify the insertion of foreign DNA into helper-independent retroviral vectors. *J. Virol.* **61**, 3004–3012 (1987).

The EMBO Journal (2009), 1–15 | © 2009 European Molecular Biology Organization | All Rights Reserved 0261-4189/09
www.embojournal.org

THE EMBO JOURNAL

MAPKAP kinase MK2 maintains self-renewal capacity of haematopoietic stem cells

Jessica Schwermann[1,4], Chozhavendan Rathinam[2,4,5], Maria Schubert[1,4], Stefanie Schumacher[1], Fatih Noyan[2], Haruhiko Koseki[3], Alexey Kotlyarov[1,4], Christoph Klein[2,4] and Matthias Gaestel[1,4,*]

[1]Institute of Biochemistry, Hannover Medical School, Hannover, Germany, [2]Department of Pediatric Hematology/Oncology, Hannover Medical School, Hannover, Germany and [3]RIKEN Research Center for Allergy and Immunology, Tsurumi-ku, Yokohama, Japan

The structurally related MAPK-activated protein kinases (MAPKAPKs or MKs) MK2, MK3 and MK5 are involved in multiple cellular functions, including cell-cycle control and cellular differentiation. Here, we show that after deregulation of cell-cycle progression, haematopoietic stem cells (HSCs) in MK2-deficient mice are reduced in number and show an impaired ability for competitive repopulation *in vivo*. To understand the underlying molecular mechanism, we dissected the role of MK2 in association with the polycomb group complex (PcG) and generated a MK2 mutant, which is no longer able to bind to PcG. The reduced ability for repopulation is rescued by re-introduction of MK2, but not by the Edr2-non-binding mutant of MK2. Thus, MK2 emerges as a regulator of HSC homeostasis, which could act through chromatin remodelling by the PcG complex.

The EMBO Journal advance online publication, 16 April 2009; doi:10.1038/emboj.2009.100
Subject Categories: signal transduction; differentiation & death
Keywords: chromatin remodelling; haematopoiesis; mouse knockout; protein kinase

Introduction

Haematopoietic stem cells (HSCs) represent the best-characterized type of adult stem cells. Profound analysis of surface antigens and established protocols to determine the self-renewal capacity and differentiation make HSCs a favourite model for stem cell biology. The complex microenvironment in the bone marrow regulates the fate of HSCs, controlling the balance between differentiation and self-renewal by providing cytokine and growth factors. However, intracellular signalling pathways involved in HSCs maintenance remain elusive. Recent studies showed controversial roles of evolutionarily conserved signalling pathways such as Smad-, Notch- and Wingless/Int(Wnt)-type (Reya *et al*, 2003; Duncan *et al*, 2005; Blank *et al*, 2006). The p38 mitogen-activated protein kinase (MAPK) pathway mainly regulates haematopoiesis by myelosuppressive cytokines that inhibit the growth of human primitive haematopoietic progenitors (reviewed in Platanias, 2003). p38 MAPK was also described to be necessary for erythropoietin expression and erythropoiesis (Tamura *et al*, 2000) and for thrombopoietin-induced self-renewal and expansion of HSCs through homeobox protein Hoxb4 (Kirito *et al*, 2003). More recently, the involvement of p38 MAPK in oxidative stress-elicited HSC depletion was shown (Ito *et al*, 2006). However, redundancy in these signalling pathways as well as the early embryonic lethality of most knockout mouse models makes the systemic analysis of the involvement of these pathways still puzzling.

The three MAPKAP kinases (MKs), MK2, MK3 and MK5, are involved in the regulation of inflammatory-cytokine production, in rearrangement of the cytoskeleton and cell migration, in cell-cycle checkpoint control, in developmental regulation, as well as in chromatin repression and remodelling (reviewed in Gaestel, 2006). Whereas the regulatory function of MKs in cytokine production is well known (Kotlyarov *et al*, 1999; Winzen *et al*, 1999), their role in controlling chromatin repression and remodelling remains elusive. Recent evidence indicates that polycomb group proteins may be targets for MK2 (Yannoni *et al*, 2004) and MK3 (Voncken *et al*, 2005). The polycomb group family, originally identified in *Drosophila melanogaster* as a repressor of homeotic genes, represents epigenetic chromatin modifiers with transcriptional silencing function (Zink and Paro, 1989; Valk-Lingbeek *et al*, 2004). In *Drosophila* and mammals, two cooperating PcG complexes have been identified (Lund and van Lohuizen, 2004). The polycomb repressive or initiation complex (PRC2), which shows histone-modifying activity, cooperates with the polycomb maintenance complex (PRC1), which interacts with modified histones to repress the expression of genes (Levine *et al*, 2004), such as the developmental regulators in murine embryonic stem cells (Boyer *et al*, 2006). In humans, PRC1 is a multiprotein complex including the human polycomb proteins HPC1–3, core proteins such as RING1A, RING1B, BMI1, as well as the early development regulator/human polyhomeotic EDR1/HPH1 and EDR2/HPH2. PcG proteins can interact with a series of additional molecules to exert control on gene expression in a highly regulated and dynamic manner (reviewed in Lund and van Lohuizen, 2004).

A crucial role of PRC1 and its individual components has been shown by analysis of mice with targeted deletion of mouse homologues of BMI1 (Bmi1), EDR1/HPH1 (Edr1/Mph1/Phc1/Rae28) and EDR2/HPH2 (Edr2/Mph2/Phc2). Bmi1-deficient mice are characterized by progressive

*Corresponding author. Institute of Biochemistry, Hannover Medical School, Carl-Neuberg-Str.1, 30625 Hannover, Germany.
Tel.: +49 511 532 2825; Fax: +49 511 532 2827;
E-mail: gaestel.matthias@mh-hannover.de
[4]These authors contributed equally to this work
[5]Present address: Department of Immunobiology, Yale University School of Medicine, New Haven, CT 06520, USA

Received: 10 October 2008; accepted: 24 March 2009

loss of HSCs and cerebellar neurons (van der Lugt *et al*, 1994). More recently, direct evidence implicated Bmi1 in the self-renewal of stem cells (Lessard and Sauvageau, 2003; Molofsky *et al*, 2003; Park *et al*, 2003). Similarly, Mph1/Rae28-deficient HSCs show decreased proliferative and self-renewal capacity (Ohta *et al*, 2002; Park *et al*, 2003). In addition to defects in the homeostasis of HSCs, PRC1 and PRC2 PcG mutant mice also suffer from lymphoid differentiation defects (reviewed in Valk-Lingbeek *et al*, 2004) and, in case of Phc2/Edr2, from changes in skeleton and premature senescence (Isono *et al*, 2005). Thus, PcG proteins play a crucial role in regulating stem cell self-renewal and differentiation (recently reviewed in Rajasekhar and Begemann, 2007).

In vitro evidence indicates that MK2 and MK3 may selectively interact with EDR2/HPH2 and target components of PRC1 (Yannoni *et al*, 2004; Voncken *et al*, 2005), suggesting a functional link between MAPKAP kinases and polycomb proteins. Here, we analyse the interaction between mouse PRC1 and MK2 and unequivocally document a role for the MK2 complex in maintaining the 'stemness' of HSCs *in vivo*.

Results

Phenotypic characterization of haematopoietic stem cells of MK2−/− mice

To numerically assess HSCs, we first quantified the Lin-(CD3ε−, CD11b−, B220−, Gr-1−, TER119−)-Sca1 + c-Kit + (LSK) population, classically defined as the HSC compartment. Compared with wild-type mice cells, LSK cells appeared to have increased in relative and absolute numbers in MK2−/− mice (Figure 1A and B). As LSK cells contain LT-HSC, ST-HSC, ELPs and multipotent progenitors, we also analysed HSCs defined by expression of SLAM family receptors (Kiel *et al*, 2005). As shown in Figure 1B and C, MK2−/− mice showed a decrease in CD150 + CD48− cells compared with wild-type control mice. Furthermore, upon staining total bone marrow with the Hoechst dye 33342, MK2−/− mice showed a five-fold reduction in side population (SP) cells, known to contain quiescent HSC (Goodell *et al*, 1996) (Figure 1D). LSK cells were further analysed for expression of CD34 and Flt3 to differentiate long-term (LT) (CD34−Flt3−)-, short-term (ST) (CD34 + Flt3−)-HSCs and multipotent progenitor cells (MPPs)(CD34 + Flt3 +). The relative proportion and absolute number of LT-HSCs are decreased in MK2−/− mice whereas these values are increased for MPPs (Figure 1E and F). To assess whether the lack of MK2 has any effects on the differentiation of HSC, we analysed erythroid, myeloid, and lymphoid cells in the bone marrow and spleen. In consistence with the results published earlier (Kotlyarov *et al*, 1999), the proportions of TER119, CD11b and Gr1 were not different between MK2−/− and control mice; furthermore, no differences were seen in phenotypic studies characterizing common lymphoid and myeloid progenitor cells (Supplementary Figures 1–5). In addition, by blood cell count we could not detect a haematopoietic failure in 4-, 8- and 12-months old mice, thus confirming data published earlier (Hegen *et al*, 2006; Jagavelu *et al*, 2007). These findings indicate that the HSC pool is significantly reduced in MK2−/− mice, whereas differentiation of HSCs and progenitor cells is not affected.

Functional characterization of MK2-deficient HSC

We hypothesized that inefficient PcG-mediated transcriptional repression may lead to a release of the actively maintained state of quiescence in HSC. This, in turn, should be associated with increased proliferative responses of HSCs to cytokines. To directly measure the HSC proliferation, we isolated LSK cells from wild-type and MK2−/− mice and cultured them in the presence of a recombinant cytokine cocktail consisting of SCF, IL3, IL6, Flt3L and TPO. As expected, MK2−/− LSK cells showed a significantly higher proliferative response as assessed by ^{3}H-thymidine incorporation (Figure 2A). We were also interested in monitoring the proliferation of different HSC sub-populations in the absence of cytokine stress *in vivo*. MK2−/− and wild-type mice were fed with BrdU for 48 h, and the BrdU incorporation into LSK cells was determined by FACS analysis. MK2−/− LT-, ST-HSCs and MPPs showed increased staining for BrdU (Figure 2B), indicating that enhanced proliferation of HSC is not only associated with cytokine exposure *in vitro* but also occurs in the physiological bone marrow environment *in vivo*.

To further assess a putative state of promoted cell-cycle progression in LSK cells, we carried out cell-cycle analysis using propidium iodide staining of *in vitro*-cultured LSK cells as well as LSK cells directly prepared from mice. In comparison with wild-type cells, MK2−/− cells showed fewer cells in G1/G0 phase and more cells in S and G2/M phases (Figure 2C), thus confirming increased cell-cycle progression in the absence of MK2. Cyclin-dependent kinase inhibitors are important mediators of cell quiescence and serve as checkpoints, restricting cell-cycle transition. P21Cip1Waf1-deficient HSCs show impaired self-renewal and increased proliferation (Cheng *et al*, 2000). To determine the expression levels of P21Cip1Waf1, we carried out RT–PCR analysis in CD150 + CD48− HSCs from MK2−/− and wild-type mice. As shown in Figure 2D, MK2−/− CD150 + CD48− HSCs show decreased abundance of p21Cip1/Waf1 mRNA, a finding in line with accelerated cell cycle progression in MK2−/− cells. Similar findings of decreased p21 mRNA level and increased cell-cycle progression were reported in Gfi1-deficient HSCs (Hock *et al*, 2004). To shed light on the molecular mechanism of reduced stem-cell quiescence, we determined expression levels of direct downstream targets of Bmi1, p16Ink4a and p19Arf. In the absence of Bmi1, repression of the Ink4a locus is relieved, resulting in expression of p16Ink4a and p19Arf (Jacobs *et al*, 1999). As shown in Figure 2E, MK2-deficient CD150 + CD48− HSCs show higher expression levels of p19Arf, whereas the expression levels of Ink4a and p27 (Kip1) were comparable to those of wildtype control cells (data not shown).

Cytokine-induced proliferation of HSC *in vitro* is associated with loss of 'stemness'. We hypothesized that the sequence of events resulting in loss of stemness might occur more rapidly in unrestricted proliferation of MK2-deficient HSC. As no phenotypic marker unequivocally reflects HSC function, we monitored the cell-surface expression of Sca1 as a surrogate parameter for early haematopoietic progenitor activity. CD150 + /CD48− HSCs from MK2−/− and wild-type mice were sorted (Figure 3A, upper panel) and cultured *in vitro* in the presence of the recombinant cytokines SCF, IL3, IL6, Flt3L, and TPO. Immediately after cell sorting, both MK2−/− and wild-type CD150 + /CD48− HSCs showed an

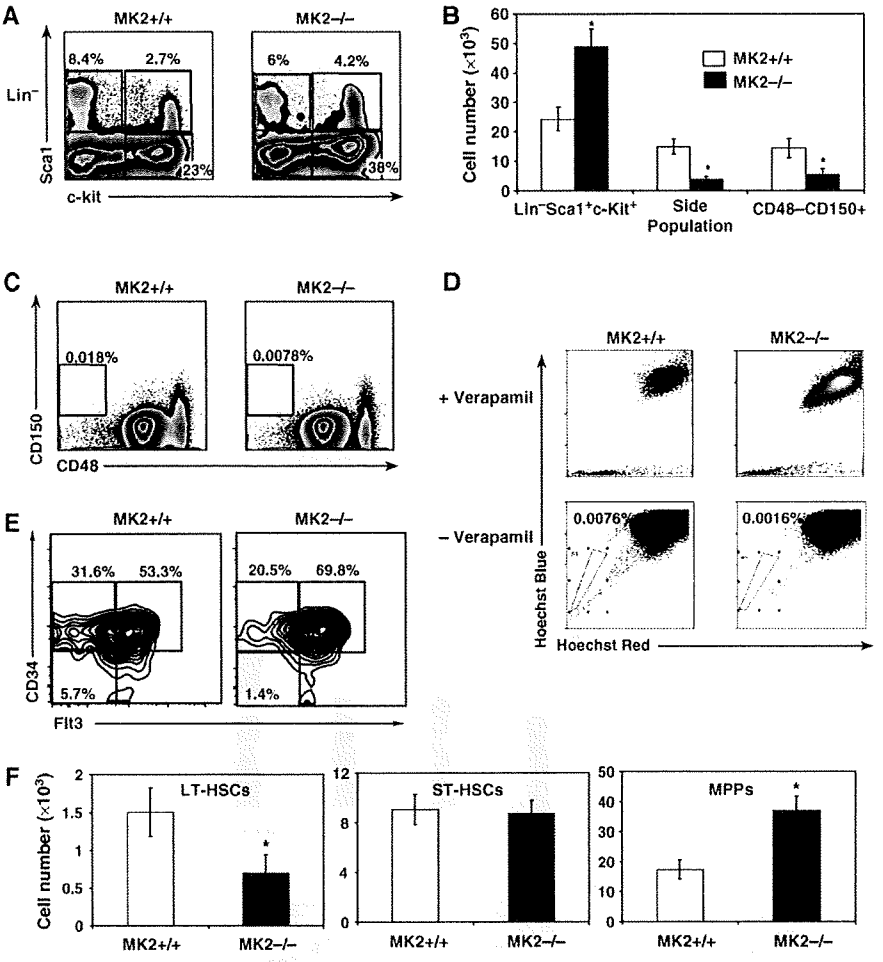

Figure 1 Phenotypic analysis of the haematopoietic stem cell compartment in MK2−/− mice. (**A**) FACS plots indicating relative increase of LSK cells in MK2−/− mice. Lineage-marker (CD3ε, CD11b, B220, Gr-1, TER119)-negative cells were gated and further analysed for expression of Sca1 and c-Kit. Data are representative of three independent experiments. (**B**) Absolute numbers of LSK, SP and CD150+ CD48− cells determined from the bone marrow of both hind limbs ($N=6$ mice). Data are representative of two independent experiments. Asterisks indicate statistical significance ($P<0.01$). (**C**) FACS plots indicating reduced frequency of CD150+ CD48− cells in MK2−/− mice. Data are representative of two independent experiments. (**D**) Side population (SP) analysis upon staining of BM cells with Hoechst 33342 dye. Cells stained with Hoechst 33342 dye in the presence of verapamil serve as controls for the specificity of the SP population. Data are representative of two independent experiments. (**E**) FACS plots indicating relative decrease of long-term (LT)-HSCs (CD34-Flt3-LSK) and short-term (ST)-HSCs (CD34+Flt3-LSK), and increase of multipotent progenitor cells (MPPs) (CD34+Flt3+LSK) in MK2−/− mice. Total BM cells of MK2+/+ and MK2−/− were prepared and stained with an antibody cocktail that recognizes lineage markers (CD11b, Gr1, B220, CD3e, TER119), Sca1 and c-Kit, and analysed by flow cytometry. LSK cells were pre-gated and further analysed for CD34 and Flt3 expression. (**F**) Absolute numbers of LT-HSCs (left), ST-HSCs (middle) and MPPs (right) determined from the bone marrow of both hind limbs ($N=5$ mice). Asterisks indicate statistical significance ($P<0.05$). Data in (E) and (F) are representative of three independent experiments.

equal pattern of expression of c-Kit and Sca1 (Figure 3A, middle panel). However, after 3 days *in vitro*, only between 16–21% of MK2−/− progenitor cells stained positive for Sca1, whereas between 60–75% of wild-type progenitor cells maintained Sca1 expression (Figure 3A, lower panel and quantification below), suggesting that MK2 is crucial for the maintenance of an early state of differentiation or quiescence. Similar results were obtained for LSK cells (data not shown). To assess whether cytokine-stimulated HSCs showed a skewed differentiation, we analysed the expression of lineage-specific cell surface markers. In comparison to wildtype cells, a larger fraction of MK2-deficient cells showed expression of CD11b and Gr1 (Supplementary Figures 6 and 7). Analysis of CD150+/CD48− HSCs using a CFSE dilution assay indicates higher proliferation of MK2-deficient cells (Figure 3B) similar to LSK cells (Figure 2A–C).

The *in vitro* culture system described above allowed us to test whether a direct inhibitor of p38 MAPK signalling similarly unleashes HSC quiescence. Wild-type LSK cells were purified and incubated for 48 h in the absence or presence of 5 μM SB239063, which does not reduce the overall viability of the cells (Supplementary Figure 8). As shown in Figure 3C, cells exposed to a specific p38 inhibitor almost completely lost the expression of Sca1, whereas cells stimulated in the absence of SB239063 remained largely positive for expression of Sca1. These findings corroborate the idea that p38 signalling is crucial for the maintenance of HSC quiescence.

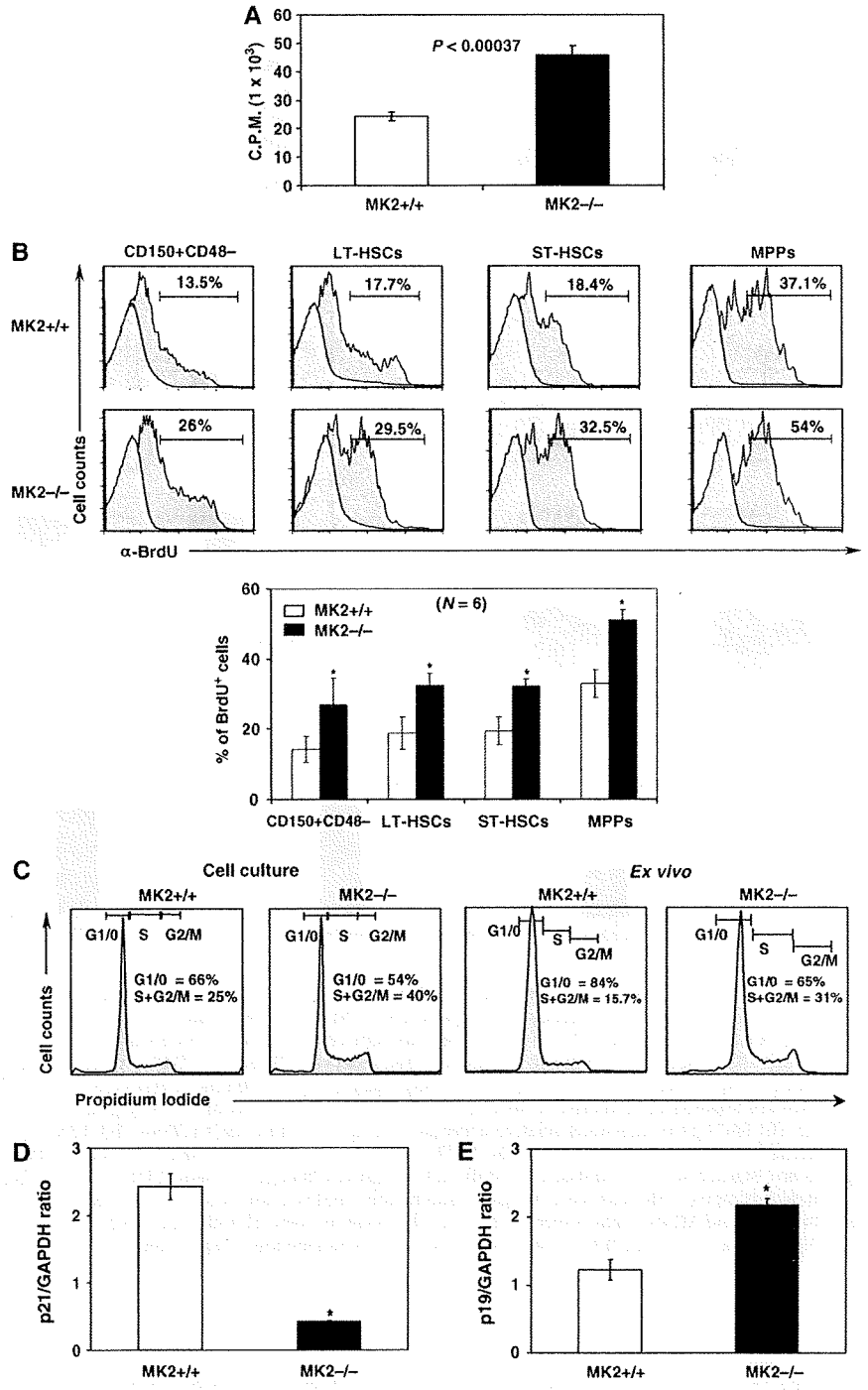

Figure 2 Increased proliferation of LSK in MK2−/− mice. (**A**) *In vitro* proliferation assay. Purified LSK cells were cultured in the presence of recombinant cytokines for 48 h, pulsed with ^{3}H-thymidine, and subjected to scintillation counting. The mean values of triplicate samples are shown. (**B**) *In vivo* BrdU incorporation experiment. The *in vivo*-proliferation potential of CD150 + CD48− cells, LT-HSCs, ST-HSCs and MPPs in MK2 + /+ and MK2−/− mice was measured after feeding BrdU through drinking water for 2 days. RBC-depleted BM cells were stained with monoclonal antibodies recognizing subsets of HSCs and BrdU (negative controls of cells from mice fed with PBS are shown as insets in light grey). Indicated HSC subsets were pre-gated and histograms were generated for quantifying the incorporated BrdU (% of BrdU-positive cells is given). Data are representative of two independent experiments. Cells from three mice from each of the two experiments were measured separately ($N = 6$). Mean and statistics are in the diagram given below (asterisks indicate significant differences with $P < 0.05$). (**C**) Cell-cycle analysis. Purified LSK cells were cultured *in vitro* in the presence of recombinant cytokines for 48 h. Cells were fixed, stained with propidium iodide and their DNA content was measured by flow cytometry (left panel). LSK cells isolated from MK2 + /+ and MK2−/− mice were sorted, directly fixed and stained with propidium iodide, and their DNA content was measured by flow cytometry (right panel). (**D**, **E**) Real-time PCR showing p21Cip1/Waf1 (D) and p19Arf mRNA levels (E) in purified CD150 + CD48−HSCs. The mean values of duplicate samples are shown. Asterisks indicate statistical significance ($P < 0.01$). Data are representative of two independent experiments each.

To directly assess the self-renewal capacity of HSC, we carried out competitive repopulation experiments. Various numbers of wild-type and MK2−/− bone marrow cells (CD45.2) were mixed with 10^5 wild-type CD45.1 competitor cells and transplanted into lethally irradiated CD45.1 recipient mice. Three months later, the mice were killed and the specific contribution of CD45.1 and CD45.2 cells to haematopoiesis was assessed by FACS analysis. In line with earlier experiments (Kotlyarov *et al*, 1999) and the data shown in Supplementary Figures 1–5, no defect of differentiation in various haematopoietic lineages could be observed in mice transplanted with MK2−/− cells (data not shown), confirming that MK2 is not crucially involved in controlling HSC differentiation. When 10^5 HSCs were mixed with 10^5 competitor cells, MK2-deficient cells contributed to 54% of haematopoiesis, whereas wild-type cells contributed to 75% of haematopoiesis. However, under limiting conditions, when fewer HSCs were transplanted, the statistically significant

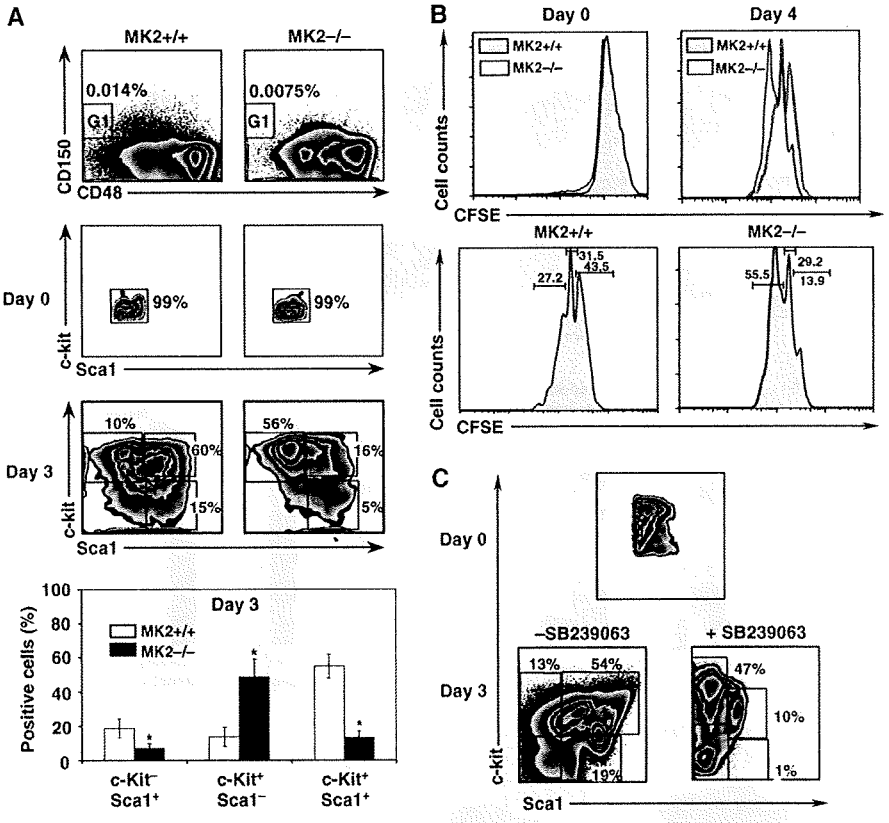

Figure 3 Compromised haematopoietic stem cell function in MK2−/− mice. **(A)** Contour plots indicating an accelerated loss of Sca1 expression in MK2−/− SLAM cells *in vitro*. The upper panel shows sorting of SLAM cells, the middle panel shows expression pattern of Sca1 and c-Kit in primary sorted SLAM cells; and the two lower panels show Sca1 and c-Kit expression after 3 days of *in vitro* culture in the presence of recombinant cytokines. Cell subsets were discriminated on the basis of differential expression of Sca1 and c-Kit, their percentages were calculated and plotted. Asterisks indicate statistical significance ($P<0.01$). Data are representative of two independent experiments. **(B)** CFSE-proliferation assay for WT and MK2-deficient SLAM cells. Sorted CD150+CD48− HSCs of MK2+/+ and MK2−/− mice were stained with CFSE and cultured *in vitro* in the presence of cytokine cocktail for 3 days. On day 4, aliquots of cells were analysed by flow cytometry. Histograms, documenting increased *in vitro* proliferation of MK2−/− CD150+CD48− HSCs, as assessed by the percentage of cells that appear under gates that measure each cycle of proliferation. **(C)** FACS plots indicating an accelerated loss of Sca1 expression in MK2+/+ cells in the presence of the MAPK p38 inhibitor SB239063. The upper panel shows the expression pattern of Sca1 and c-Kit in primary sorted LSK cells, lower panels show Sca1 and c-Kit expression after 3 days *in vitro* culture containing recombinant cytokines in the presence or absence of SB239063, respectively. Data are representative of two independent experiments. **(D)** Competitive repopulation experiment. 10^5 CD45.1$^+$ competitor BM cells were mixed with defined numbers of CD45.2+ MK2+/+ or CD45.2+ MK2−/− BM cells, and total BM was analysed for competitive repopulation as described. A characteristic experiment (left) and statistical evaluation (right) ($N=5$) are shown. Asterisks indicate statistically significant ($P<0.05$, single sided *t*-test) differences between MK2-deficient and wildtype cells. **(E)** Competitive repopulation assay as in (D), but using 10^4 CD45.1+ competitor LSK cells mixed with defined numbers of CD45.2+ MK2+/+ or CD45.2+ MK2−/− LSK cells in lethally irradiated (9.5 Gy) CD45.1+ congenic recipients. A characteristic experiment (left) and statistical evaluation (right) ($N=10$) are shown. Asterisks indicate statistically significant ($P<0.05$, single-sided *t*-test) differences between MK2-deficient and wildtype cells. **(F)** Secondary transplantation of 2×10^6 WT and MK2−/− bone marrow cells (CD45.2) mixed with 10^5 competitor cells. Analysis was performed 16 weeks after transplant. A characteristic experiment (left) and statistical evaluation (right) ($N=5$) are shown. Asterisks indicate statistically significant ($P\leqslant0.05$, single-sided *t*-test) differences between MK2-deficient and wildtype cells. **(G)** FACS plots and quantification indicating reduced frequencies of CD150+CD48− HSCs in CD45.1 WT congenic recipients that received MK2−/− LSK cells. Sorted LSK (CD45.2) cells of MK2+/+ and MK2−/− mice were transplanted into lethally irradiated CD45.1 wildtype recipients. At 16 weeks after transplantation, donor-derived (CD45.2) haematopoietic cells of BM were pre-gated and analysed for CD150 and CD48 expression (left). Absolute numbers of donor (CD45.2)-derived CD150+ CD48− cells were determined from the bone marrow of both hind limbs ($N=5$ mice). The asterisk indicates statistically significance ($P<0.05$). Data are representative of two independent experiments.